Structural variability, coordination, and adaptation of a native photosynthetic machinery

Long-Sheng Zhao[1,2,3,4], Tuomas Huokko[2], Sam Wilson[5], Deborah M. Simpson[2], Qiang Wang[6], Alexander V. Ruban[5], Conrad W. Mullineaux[5], Yu-Zhong Zhang[1,3,4,*], Lu-Ning Liu[2,3,*]

[1] State Key Laboratory of Microbial Technology, and Marine Biotechnology Research Center, Shandong University, Qingdao 266237, China.
[2] Institute of Integrative Biology, University of Liverpool, Liverpool L69 7ZB, United Kingdom
[3] College of Marine Life Sciences, and Frontiers Science Center for Deep Ocean Multispheres and Earth System, Ocean University of China, Qingdao 266003, China
[4] Laboratory for Marine Biology and Biotechnology, Pilot National Laboratory for Marine Science and Technology, Qingdao 266237, China
[5] School of Biological and Chemical Sciences, Queen Mary University of London, Mile End Road, London E1 4NS, United Kingdom
[6] State Key Laboratory of Crop Stress Adaptation and Improvement, School of Life Sciences, Henan University, Kaifeng 475004, China

*Corresponding authors: luning.liu@liverpool.ac.uk (L.-N.L.), zhangyz@sdu.edu.cn (Y.-Z.Z.)

Abstract: Cyanobacterial thylakoid membranes represent the active sites for both photosynthetic and respiratory electron transport. We used high-resolution atomic force microscopy to visualise the native organisation and interactions of photosynthetic complexes within the thylakoid membranes from the model cyanobacterium *Synechococcus elongatus* PCC 7942. The thylakoid membranes are heterogeneous and assemble photosynthetic complexes into functional domains to enhance their coordination and regulation. Under high light, the chlorophyll-binding proteins IsiA are strongly expressed and associates with Photosystem I (PSI) forming highly variable IsiA−PSI supercomplexes to increase the absorption cross-section of PSI. There are also tight interactions of PSI with Photosystem II (PSII), cytochrome b_6f, ATP synthase, and NAD(P)H dehydrogenase complexes. The organisational variability of these photosynthetic supercomplexes permits efficient linear and cyclic electron transport and bioenergetic regulation. Understanding the organisational landscape and environmental adaptation of cyanobacterial thylakoid membranes may help inform strategies for engineering efficient photosynthetic systems and photo-biofactories.

Introduction

Phototrophic prokaryotes have evolved intracytoplasmic membranes to maximise photosynthetic light absorption and fulfil energy transduction. A superior example of bacterial intracytoplasmic membranes is the thylakoid membrane found in most cyanobacteria[1], which represents one of the most important and complicated membrane systems in nature[2,3].

The cyanobacterial thylakoid membrane is densely packed by various membrane protein complexes that are responsible for both photosynthetic and respiratory electron transport[1]. Photosynthetic electron transport is carried out mainly by four membrane-spanning macromolecular complexes, photosystems I (PSI), photosystems II (PSII), cytochrome b_6f complex (Cyt b_6f) and ATP synthase (ATPase), homologous to the photosynthetic complexes in chloroplasts. The main light-harvesting antenna for PSII in cyanobacteria is the phycobilisome, a large pigment-binding macromolecular complex associated with the thylakoid membrane[1,4]. There is also a membrane-spanning protein associated with PSI, known as IsiA, which is expressed under stress conditions[5-10]. However, the role of IsiA is still unclear. It has been proposed to function as an accessory antenna for PSI. Recent electron microscopy revealed that each IsiA monomer coordinates 17 chlorophyll (Chl) molecules and 18 IsiA can encircle a PSI trimer to form an IsiA−PSI supercomplex[11,12]. Thus, the IsiA−PSI supercomplex exhibits an 81% increase of optical cross-section and enhanced energy transfer compared to PSI trimer alone[13,14]. PSI can also be surrounded by two IsiA rings, 18 IsiA monomers in the first ring and 25 in the second ring, forming a larger IsiA−PSI supercomplex[15]. Other proposed roles of IsiA are an energy dissipator for photoprotection[9,16] and Chl storage[17]. Additionally, cyanobacterial thylakoid membranes also accommodate components of the respiratory electron transport chains, comprising type-I NAD(P)H

dehydrogenase (NDH-1), succinate dehydrogenase, and terminal oxidases[2,3]. The intricate organisation, functional links, and regulation of different electron transport complexes in the thylakoid membrane are critical for cyanobacterial bioenergetics and growth in varying ecophysiological environments.

Despite substantial information about the structures and functions of individual bioenergetic complexes, our knowledge about how these electron transport complexes are organised and physiologically coordinated with others in native thylakoid membranes remains primitive. The cyanobacterial thylakoid membrane network is laterally heterogeneous, resembling plant chloroplast and mitochondrial membranes[18]. Using fluorescent tagging, recent studies have demonstrated the heterogeneous distribution of photosynthetic complexes in thylakoid membranes from the model cyanobacterium *Synechococcus elongatus* PCC 7942 (Syn7942)[19] and the lateral segregation of PSI in *Synechocystis* sp. PCC 6803 (Syn6803)[20]. The complexity of cyanobacterial thylakoid membranes features the formation of photosynthetic megacomplexes to facilitate defined electron transfer pathways[21,22].

Atomic force microscopy (AFM) has become a unique and powerful tool in studying membrane protein structure, organisation, and dynamics in photosynthetic membranes at the near-physiological context[23]. AFM possesses a high signal-to-noise ratio, thus with no requirement for data averaging, and permits direct visualisation of membrane proteins in the native environment in solution, avoiding complex purification and detergent treatment. Medium-resolution AFM images have revealed the PSI organisation and intermixture of PSI, PSII, and Cyt b_6f complexes in the thylakoid membranes from various cyanobacterial species[19,20,24]. However, the lateral associations and structural adaptation of the electron transport supercomplexes in cyanobacterial thylakoid membranes are still missing.

Here, we apply high-resolution AFM imaging to draw a landscape view of the native arrangement of membrane complexes in the thylakoid membrane from Syn7942. Our results provide novel insight into the heterogeneity, compartmentalisation and functional regulation of cyanobacterial photosynthetic apparatus, which is extendable to other membrane systems in bacteria, chloroplasts, and mitochondria. The naturally occurring organisational features of thylakoid membranes could be important considerations for the future engineering of artificial photosynthetic systems to underpin biofuel production.

High light induces IsiA expression and formation of the IsiA−PSI supercomplex

The transcription of the IsiA-encoding gene (*isiA*) is regulated by two transcription factors, RpaB (regulator of phycobilisome association B) and Fur (Ferric Uptake Regulator)[25]. RpaB controls the transcription of photosynthesis-associated genes in response to light[25]. Its binding motif, a high-light regulatory (HLR) sequence, is at upstream of many high-light-inducible genes including *isiA* (Supplementary Fig. 1a)[25,26]. Fur is could repress *isiA* expression under iron-replete condition, by binding the Fur box region of *isiA* (Supplementary Fig. 1a)[8]. These facts suggest that the expression of *isiA* could be regulated by both iron availability and light intensity.

The thylakoid membranes were isolated from the wild-type (WT) Syn7942 cells grown under moderate light (ML, 40 μmol photons m^{-2} s^{-1})[27-29], high light (HL, 300 μmol photons m^{-2} s^{-1}), or iron deficiency (Fe-), using low ion-concentration buffers in the absence of any detergents. This allowed us to obtain large thylakoid membranes with the size of up to 1 μm[19], which are mostly free of phycobilisomes (disassociated from the thylakoid membrane and disassembled in low ion-concentration buffers), ideal for the long-range membrane organisation imaging by AFM. Absorption spectra (Supplementary Fig. 1), mass spectrometry, and sodium dodecyl sulfate polyacrylamide gel electrophoresis (SDS-PAGE) combined with immunoblot analyses (Supplementary Fig. 2) confirmed that both HL and iron-deficiency treatments could induce IsiA expression, leading to the elevated IsiA content in Syn7942 thylakoids. The IsiA amount in the Fe- adapted thylakoid membranes was about 4.5-fold higher than that in the HL-adapted membranes (Supplementary Fig. 2a). By contrast, the PSI content relative to the total thylakoid protein content in thylakoid membranes was reduced under both HL and iron deficiency (Supplementary Fig. 2a, 2b). These changes led to an increased IsiA:PSI ratio in the HL- and Fe- thylakoid membranes. Blue native polyacrylamide gel electrophoresis (BN-PAGE) and immunoblot analysis further indicated that IsiA could bind with PSI to form IsiA−PSI complexes (Supplementary Fig. 2d, 2e). The PSII and Cyt b_6f content was decreased under HL, similar to PSI, but was slightly increased under Fe- compared to ML (Supplementary Fig. 2a). The PSII dimer:monomer ratio was relatively similar between Fe- and ML conditions and was reduced under HL (Supplementary Fig. 2f). The amount of ATPase was constant under ML and HL (Supplementary Fig. 2a, 2c) and was elevated under Fe- compared to that under ML (Supplementary Fig. 2a).

We performed high-resolution AFM imaging on the isolated thylakoid membranes to dissect the native structures and membrane organisation of bioenergetic supercomplexes. AFM topographs showed that membrane proteins were densely packed in both ML- and HL-adapted thylakoid membranes (Fig. 1a, 1b, 1e,

1f). ML-adapted thylakoid membrane contains predominately the trimeric structures (triangles), as well as some dimeric (oval) and monomeric features (square) (Fig. 1c). The trimeric structure has the protruding height of 2.58 ± 0.16 nm (n = 30) above membrane surface and possesses a three-fold rotational symmetry, with the angle between the long axes of the three protrusions of approximately 120°, consistent with the characteristic cytoplasmic-side structure (referring to PsaC, PsaD, and PsaE subunits) of cyanobacterial PSI trimers (Fig. 1d)[19,30]. Thus, these trimeric structures were assigned to be PSI trimers. PSI trimers have no specific orientation and coexist with PSI dimers and monomers in the Syn7942 thylakoid membranes (Fig. 1c). Diverse arrangement patterns of PSI trimers were identified in the ML-adapted thylakoid membranes (Supplementary Fig. 3), indicative of the aggregation flexibility of PSI complexes. This may provide a means for adjusting PSI contents per membrane area to regulate photosynthetic electron transport.

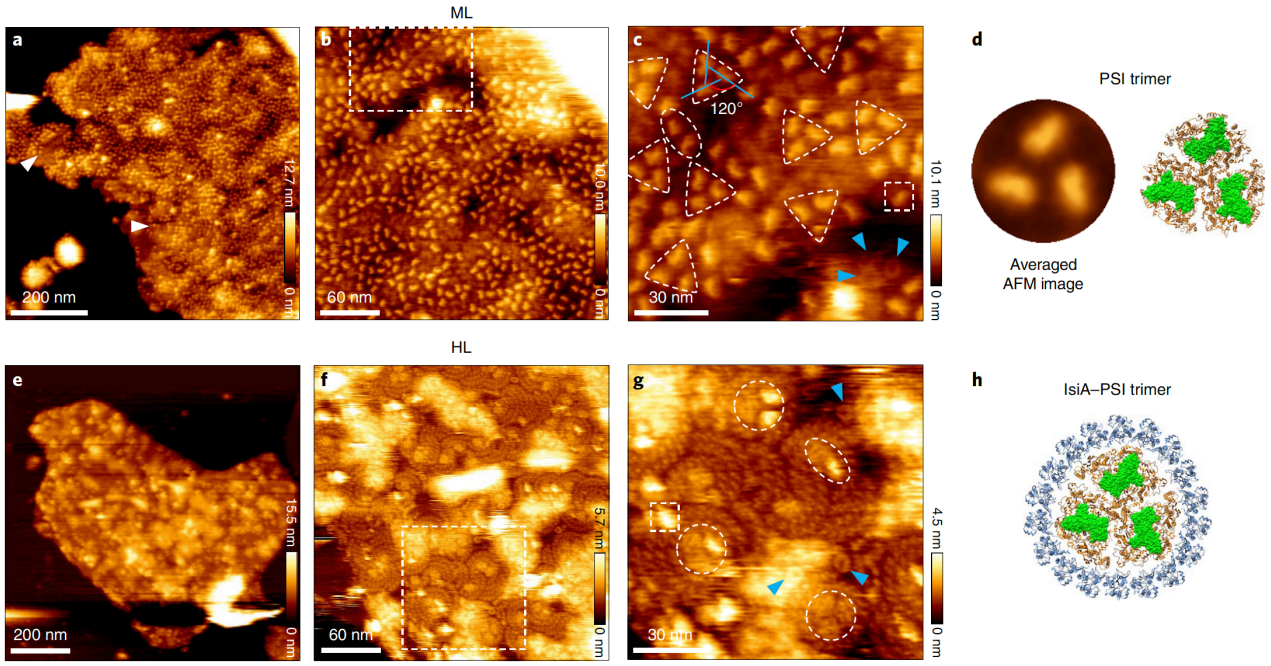

Fig. 1 | AFM images of native thylakoid membranes from ML- and HL-adapted Syn7942 cells. a, AFM topograph of ML-adapted thylakoid membrane fragment in liquid showing the densely packed photosynthetic membrane proteins. Structures with ordered organization are indicated by arrowheads. **b**, High-resolution AFM image of the cytoplasmic surface of a ML thylakoid membrane showing more clearly the crowded arrangement of photosynthetic membrane proteins. The area represented by the white box is shown in **c**. **c**, Zoomed-in view of the area highlighted in **b** showing in detail the trimeric (triangle), dimeric (oval) and monomeric (square) PSI complexes. The angle between the long axes of the three protrusions is denoted by solid blue lines. Small ring-like structures, speculated to be ATPase membrane domains, are indicated by blue arrowheads. **d**, Threefold symmetrized and correlation-averaged AFM topograph of PSI from the cytoplasmic surface of thylakoid membranes (left). Atomic structure of the trimeric PSI complex from the cytoplasmic surface (right, PDB: 1JB0). The subunits (PsaC, PsaD and PsaE) in green are domains protruding above the membrane surface. **e**, AFM topograph of HL-adapted thylakoid membrane fragment in liquid. **f**, High-resolution AFM image of the cytoplasmic surface of HL thylakoid membrane showing more clearly the densely packed photosynthetic membrane proteins. The area delineated by the white box is shown in **g**. **g**, Zoomed-in view of the area highlighted in **f** showing the trimeric (circle), dimeric (oval) and monomeric (square) PSI complexes in more detail. Small ring-like structures, speculated to be ATPase membrane domains, are highlighted with blue arrowheads. **h**, Atomic structure of the IsiA–PSI supercomplex from the cytoplasmic surface (PDB: 6NWA). The subunits (PsaC, PsaD and PsaE) in green are domains protruding above the membrane surface. Representative AFM imaging was derived from a minimum of five biologically independent membrane preparations.

Compared to the ML-adapted thylakoid membranes, HL results in the reduction of the PSI content (69%) and the proportion of PSI trimers in the total PSI in the HL-adapted membranes (Supplementary Table 1). PSI complexes (circles) were less densely distributed in the HL-adapted thylakoid membranes and were laterally separated from their neighbouring PSI by proteins that are remarkably smaller than PSI monomers (Fig. 1e, 1f, 1g, Supplementary Table 1). These proteins form ring-like or arc structures around PSI to construct PSI-centred supramolecular assemblies (Fig. 1g), resembling the IsiA–PSI complexes from iron-limited cyanobacteria (Fig. 1h)[6,7,11,12]. The overall height of IsiA proteins is 4.3 ± 0.1 nm (n = 5), less than that of PSI without PsaC, PsaD, and PsaE (5.0 ± 0.1 nm, n = 15) (Supplementary Fig. 4). These results revealed that HL, which has notable impacts on the organisations of thylakoid membrane complexes and CO_2-fixing organelles of Syn7942[19,27-29], could induce the biosynthesis of IsiA to become the major proteins in cyanobacterial thylakoid membranes and form IsiA–PSI supercomplexes.

In addition, some structures with an ordered organisation (Fig. 1a, white arrows) and ring structures (Fig. 1c, 1g, blue arrows) were tentatively identified as PSII and ATPase complexes, respectively (see detailed analysis below).

Nanodissection of PSI subunits

Continuous AFM imaging on the same membrane with gentle scanning force (< 100 picoNewton) resulted in the removal of strongly-protruded PsaC, PsaD, and PsaE subunits from intact PSI (Fig. 2a, 2b), indicative of their weak interactions with the PSI base at the cytoplasmic side. Figs. 2c and 2d display the representative images of the PSI trimers before and after the PSI protrusions were dissected by the AFM probe (arrows). The distance between two protrusions within the PSI trimer is 10.3 ± 1.0 nm (Fig. 2e, 2f), consistent with that determined from the crystal structure of PSI trimers (11 nm, PDB: 1JB0)[30] (Fig. 2g). The height of the protrusion structures is 2.0 ± 0.3 nm, in agreement with the heights of PsaC, PsaD, and PsaE subunits (2.6 nm) (Fig. 2g). Removal of PsaC, PsaD, and PsaE permitted visualisation of the fine surface textures of PSI underneath these subunits in great details (Fig. 2h). Three "ridges" on the surface of each monomer were discerned, in line with the cytoplasmic structure of PSI monomers without PsaC, PsaD, and PsaE (Fig. 2i), further confirming that these strongly protruded features were PSI complexes.

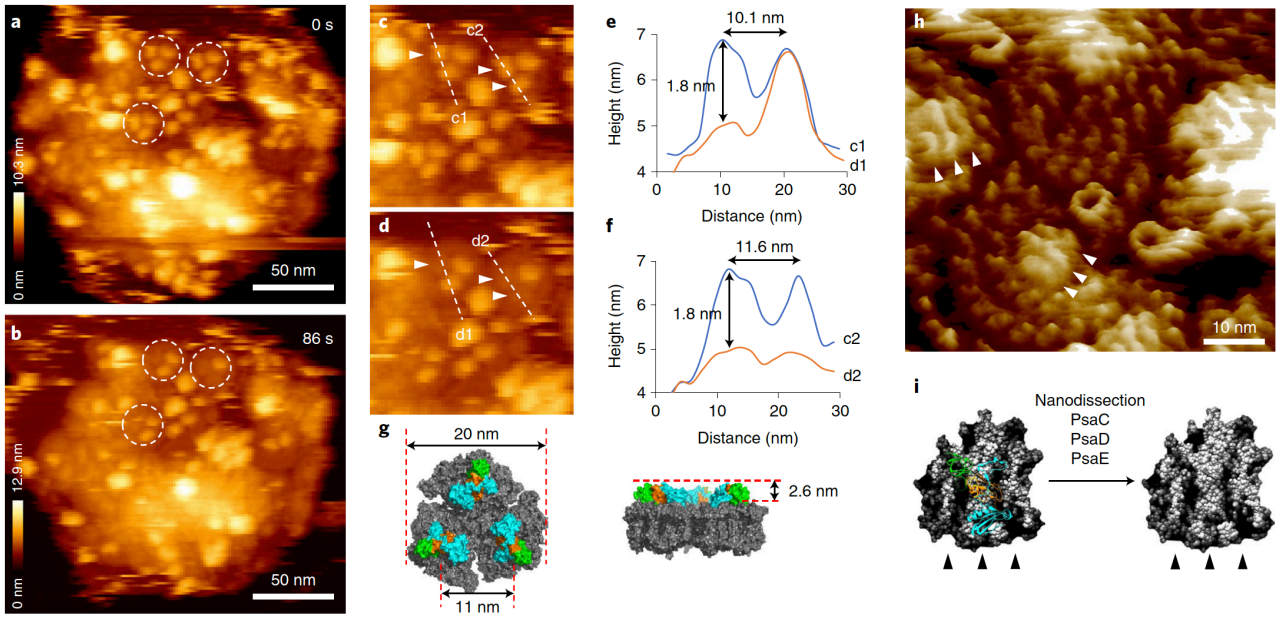

Fig. 2 | Removal of the cytoplasmic subunits of PSI by AFM nanodissection. a, The first scan of a HL-adapted thylakoid membrane fragment by AFM. Trimeric PSI complexes are highlighted with circles. **b**, Second scan of the fragment shown in **a**. The same trimeric PSI complexes are also highlighted with circles. **c**, Zoomed-in view of the three trimeric PSI complexes circled in **a**. Dashed lines show the positions of height profiles and arrowheads represent three protrusions of PSI complexes. **d**, Zoomed-in view of the three trimeric PSI complexes circled in **b**. Dashed lines show the positions of height profiles shown in **c**. Protrusions of PSI complexes indicated by arrows in **c** were removed. **e**, Height profiles corresponding to the c1 line in **c** and d1 line in **d**. The lateral distance between peaks is 10.1 nm, and the height difference in the PSI complex before and after loss of subunits is 1.8 nm. **f**, Height profiles corresponding to the c2 line in **c** and d2 line in **d**. The lateral distance between peaks is 11.6 nm, and the height difference in the PSI complex before and after loss of subunits is 1.8 nm. **g**, Atomic structure of the trimeric PSI complex from the cytoplasmic surface (PDB: 1JB0). The diameter of the trimeric PSI complex is 21 nm. The distance between the highest positions of PSI monomers is 11 nm, and the height of the subunits (PsaC (orange), PsaD (blue) and PsaE (green)) above the membrane surface is 2.6 nm. **h**, High-resolution AFM image of the cytoplasmic surface of HL-adapted thylakoid membrane showing in detail the PSI surface structure after loss of subunits (arrowheads). **i**, Atomic structure of the monomeric PSI complex from the cytoplasmic surface (PDB: 1JB0). PsaC (orange), PsaD (blue) and PsaE (green) subunits have been removed, and three ridges appear as indicated by black arrowheads. Representative AFM imaging was derived from at least five biologically independent membrane preparations.

Distribution and structural heterogeneity of IsiA–PSI supercomplexes in thylakoid membranes

AFM topographs showed that a typical IsiA–PSI trimer complex possesses a round structure with three-fold rotational symmetry (Fig. 3a); eighteen IsiA monomers form a ring encompassing the PSI trimer, in close agreement with the cryo-electron microscopy (cryo-EM) structure of IsiA–PSI trimers (PDB: 6NWA)[11] and the simulated AFM image based on the cryo-EM structure (Fig. 3a). Contrary to the homogeneous structure obtained from averaged EM images[6,7,11,12,15,31], AFM images revealed the inherent structural variability of IsiA–PSI supercomplexes in native thylakoid membranes (Fig. 3b-3f, Supplementary Figs. 5, 6). PSI trimers, dimers, and monomers can be encircled by IsiA single, double, triple, or multimeric rings, respectively, forming diverse IsiA–PSI structures varying in dimension (Fig. 3b, Supplementary Fig. 5). Approximately 71% of the IsiA–PSI supercomplexes possessed one IsiA ring and as the number of rings increased the content of corresponding supercomplexes decreased gradually (Supplementary Table 2). The distribution and orientation of diverse IsiA–PSI supercomplexes were readily random (Fig. 3c-3f, Supplementary Fig. 6).

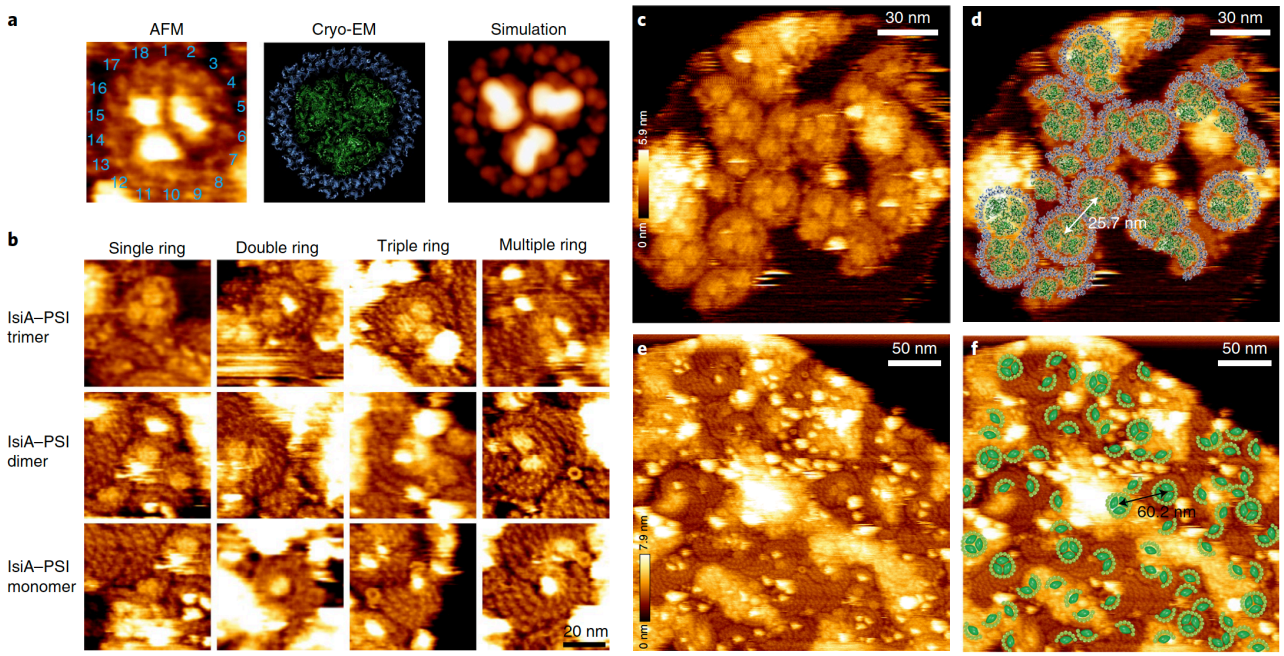

Fig. 3 | AFM topographs of thylakoid membranes from HL-adapted Syn7942 cells. a, Zoomed-in view of AFM topograph of IsiA–PSI trimer supercomplex showing 18 IsiA subunits around the PSI trimer (left). Atomic structure of the IsiA–PSI supercomplex from the cytoplasmic surface (middle, PDB: 6NWA). Simulated AFM image of IsiA–PSI supercomplex based on PDB: 6NWA (right). **b**, IsiA–PSI supercomplexes with various numbers of IsiA rings and different PSI oligomerization states. **c**, AFM topograph of HL-adapted thylakoid membrane fragment with densely packed IsiA–PSI supercomplexes. **d**, Structural model of the arrangement of IsiA–PSI supercomplexes within the thylakoid membrane in **a** (PDB: 6NWA). The distance between two adjacent IsiA–PSI trimer supercomplexes is 25.7 nm. **e**, AFM topograph of HL-adapted thylakoid membrane fragment with densely packed IsiA proteins. PSI complexes are interspersed throughout the membrane. **f**, Model of the arrangement of IsiA–PSI supercomplexes within the thylakoid membrane in **c**. The distance between two close IsiA–PSI trimer supercomplexes is 60.2 nm. Representative AFM imaging was derived from at least five biologically independent membrane preparations.

The first closed IsiA ring associated with PSI commonly consists of 18 peaks of IsiA monomers (Fig. 4a), consistent with the EM results[6,7,11,12,15] (Fig. 1h). The average distance between adjacent IsiA protrusions in the first ring enclosing the PSI trimer is 4.5 ± 0.1 nm (n = 160), larger than those within the second (4.2 ± 0.1 nm, n = 91), the third (4.2 ± 0.2 nm, n = 17), the fourth rings (4.2 ± 0.1 nm, n = 5), and IsiA-only assemblies (4.2 ± 0.1 nm, n = 104) (Fig. 4a, 4b, 4c). Regardless of the oligomeric states of PSI, the IsiA intervals within the second, third or fourth ring, as well as in the IsiA-only assemblies are similar, but in all above it is less than that in the first ring that directly contacts PSI (Two-sided two-sample t-Test, $p < 0.001$) (Fig. 4c). These results suggested that the binding between IsiA and PSI can modify the lateral arrangement of IsiA in the membrane. The smaller space between adjacent IsiA at the peripheral rings may facilitate excitation energy transfer between Chls of neighbouring IsiA proteins within the same ring, whereas the larger space between adjacent IsiA in the first ring that directly contacts PSI may weaken energy transfer between IsiA subunits and favour energy transfer towards the central PSI. In addition, the first IsiA rings are often intact, whereas complete IsiA circles were barely seen in the following rings as well as the first ring that encircles PSI dimers and monomers, confirming the importance of binding with PSI trimers in shaping IsiA assemblies. The distances between the inner and outer rings of IsiA–PSI double-ring and triple-ring complexes as well as between adjacent rings of the IsiA-only assemblies are relatively identical (5.0 ± 0.2 nm, n = 18) (Fig. 4d), probably essential for efficient energy transfer. Based on the AFM results and cryo-EM of the IsiA–PSI supercomplex, the structural models of the PSI trimer associated with IsiA double rings and triple rings were built (Fig. 4e).

Strikingly, IsiA proteins could also self-assemble to form, for example, a helical "stripe" surrounding the central PSI (Supplementary Fig. 7a), the "S-shape" fibres formed by IsiA oligomers to connect two adjacent IsiA–PSI supercomplexes (Supplementary Fig. 7b), the "storm-like" IsiA assemblies around one PSI (Supplementary Fig. 7c), and the insertion of IsiA fibres into the centre of adjacent IsiA–PSI supercomplex through the gap among IsiA assemblies (Supplementary Fig. 7d). The highly variable structures of IsiA assemblies in nature may suggest the plastic IsiA–IsiA and IsiA–PSI interactions *in vivo* and the sequential multistep formation of the IsiA–PSI supercomplex.

Structural variability of IsiA–PSI supercomplexes in the iron-starved thylakoid membranes

To investigate whether the organisational heterogeneity of IsiA–PSI supercomplexes in thylakoid membranes is specific to HL adaptation or it also occurs in iron-deficiency conditions, we conducted AFM imaging on the

Fe- adapted thylakoid membranes. Consistent with the organisation of the HL-adapted thylakoid membranes, IsiA proteins were densely packed in the Fe- adapted thylakoid membranes and formed various IsiA–PSI supercomplexes that differ in the number of IsiA rings and PSI oligomeric states (Supplementary Fig. 8), indicating that the structural variability is a generic feature of IsiA–PSI assemblies under different stress conditions. The proportion of IsiA–PSI supercomplexes surrounded by a single IsiA ring was declined in the Fe- adapted membranes compare to the HL-adapted membranes, while the proportion of IsiA–PSI supercomplexes with more IsiA rings was increased (Supplementary Table 2), due to the drastic increase of IsiA abundance in the Fe- adapted thylakoid membranes (Supplementary Fig. 2a, 2b). The higher expression of IsiA under iron starvation compared to HL also led to the formation of more IsiA-enriched assemblies in thylakoid membranes (Supplementary Fig. 8).

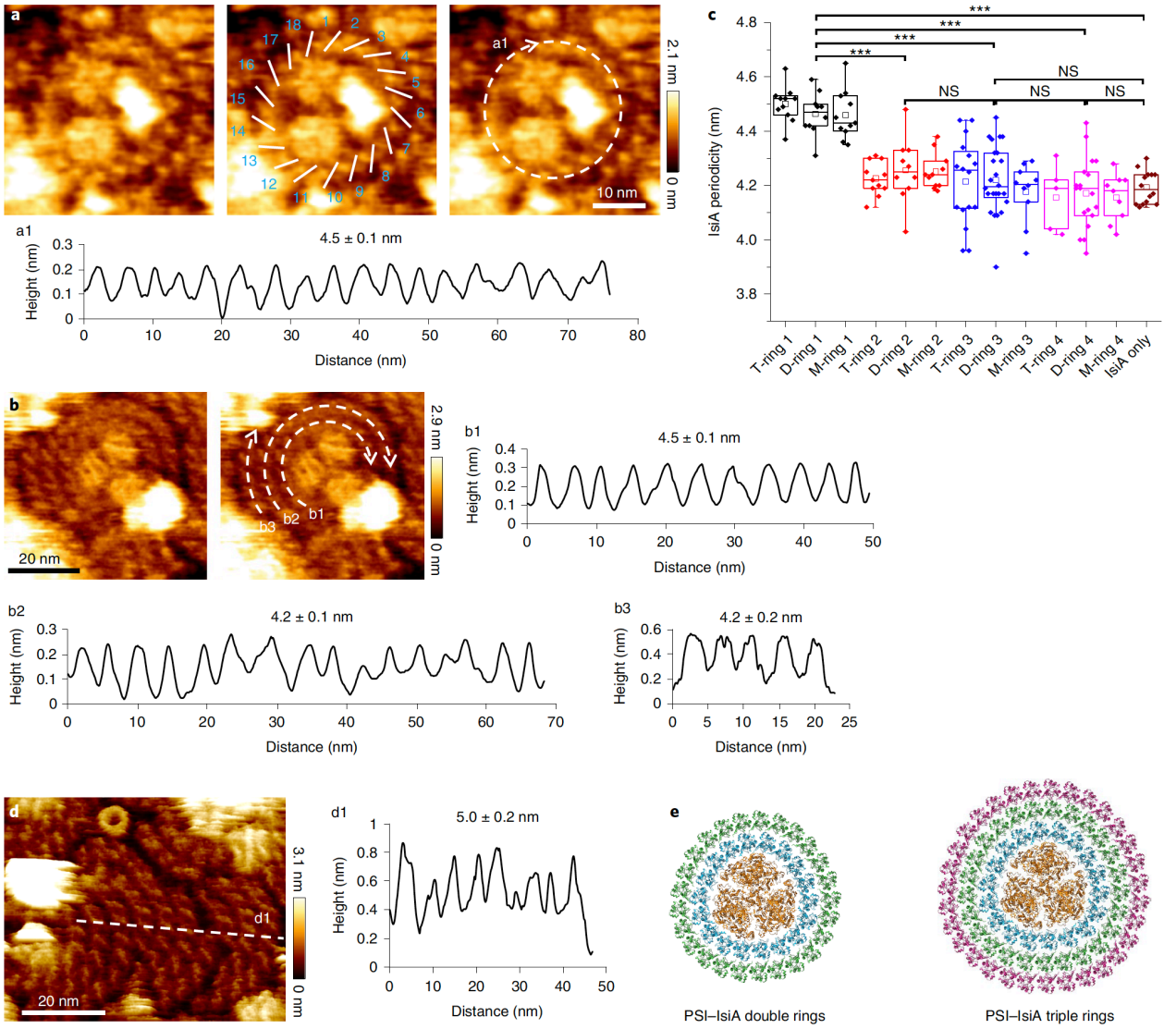

Fig. 4 | Analysis of IsiA organization. a, Zoomed-in view of an IsiA–PSI supercomplex in which the first IsiA ring is intact. Distances between IsiA monomers are indicated by white bars, and 18 IsiA subunits were identified. Height profile a1 is denoted by the dashed circle. The periodicity of IsiA in IsiA rings is 4.5 ± 0.1 nm (n = 160 calculated distances between adjacent IsiA subunits). **b**, Zoomed-in view of an IsiA–PSI supercomplex with three incomplete IsiA rings. Height profiles b1, b2 and b3 correspond to the dashed lines b1, b2 and b3, respectively. The periodicity of IsiA in the inner, middle and outer IsiA rings is 4.5 ± 0.1 nm (n = 160 calculated distances between adjacent IsiA subunits), 4.2 ± 0.1 nm (n = 91 calculated distances between adjacent IsiA subunits) and 4.2 ± 0.2 nm (n = 17 calculated distances between adjacent IsiA subunits), respectively. **c**, Box plots of IsiA periodicity in IsiA rings around PSI trimer (T), dimer (D) and monomer (M) and in IsiA self-assemblies. The numbers represent the positions of rings, counting from PSI. Box plots display the median (line), the average (open square), the interquartile range (box) and the whiskers (extending 1.5 times the interquartile range). The number of calculated distances between adjacent IsiA subunits for each ring type (from left to right) is 160, 92, 73, 91, 98, 101, 17, 24, 62, 5, 19, 55 and 104, respectively. Statistical analysis was performed using a two-sided, two-sample t-test, $^{***}P < 0.001$ (from left to right, $P = 6.51 \times 10^{-17}$, 2.68×10^{-15}, 4.75×10^{-19} and 2.20×10^{-15}, respectively). $P_{(\text{ring 2-3})} = 0.07$, $P_{(\text{ring 3-4})} = 0.32$, $P_{(\text{ring 4-IsiA only})} = 0.39$, $P_{(\text{ring 3-IsiA only})} = 0.93$. NS, not significant. **d**, Zoomed-in view of IsiA self-assembly (three-dimensionally enhanced) showing IsiA fibres in more detail. Height profile d1 corresponds to the dashed line d1. The periodicity of IsiA fibres is 5.0 ± 0.2 nm (n = 18 calculated distances between adjacent IsiA fibres). **e**, Structural models of IsiA–PSI supercomplexes with double and triple rings constructed based on cryo-EM structure (PDB: 6NWA) and AFM periodicity analysis. Representative AFM imaging was derived from at least five biologically independent membrane preparations.

Physiological roles of IsiA

To investigate the function of IsiA, we monitored the P700 oxidation kinetics of Syn7942 cells grown under ML, HL, and Fe- conditions. The *k*-values of the HL-and Fe- grown cells, which correlate with the PSI absorption cross-section[32,33], were similar and were ~25% higher than the *k*-value of the ML-grown cells (Fig. 5a), indicating that the binding of IsiA to PSI increased the absorption cross-section and antenna size of PSI complexes. The maximum amount of photo-oxidised P700 (P_m) of the HL- and Fe- grown cells were both lower than that of the ML-grown cells (Fig. 5b), and the changes in P_m is roughly consistent with the changes in PSI content under the corresponding conditions (Supplementary Fig. 2a, 2b), implying the main role of the PSI-associated IsiA in photosynthetic light harvesting. Moreover, 77K fluorescence emission spectra (excited at 435 nm) of the HL-grown cells showed a peak at 720 nm corresponding to PSI (Fig. 5c), further confirming the light-harvesting function of IsiA under HL. 77K emission spectra (excited at 435 nm and 600 nm) also revealed that the Fe- grown cells exhibit a fluorescence peak at 685 nm (Fig. 5c, 5d), representing IsiA accumulation[34]. As a higher amount of IsiA were expressed under Fe- than ML and HL (Supplementary Fig. 2a, b), we assume that the notable IsiA fluorescence could originate from the excess pool of bioenergetically-decoupled IsiA that are located at the periphery of IsiA–PSI supercomplexes or IsiA-only assemblies (Supplementary Fig. 8, Supplementary Table 2). We also found that cells that lack IsiA grew slower than the Syn7942 WT when transferred from ML to HL (Supplementary Fig. 9). Together, our data indicate that the IsiA proteins that strongly bind with PSI function as an antenna to increase PSI absorption cross-section, consistent with *in vitro* measurements[12], whereas the IsiA proteins that are far from PSI are functionally decoupled with PSI and highly fluorescent, and thus might have the function of Chl storage during the loss of photosystems under stress conditions.

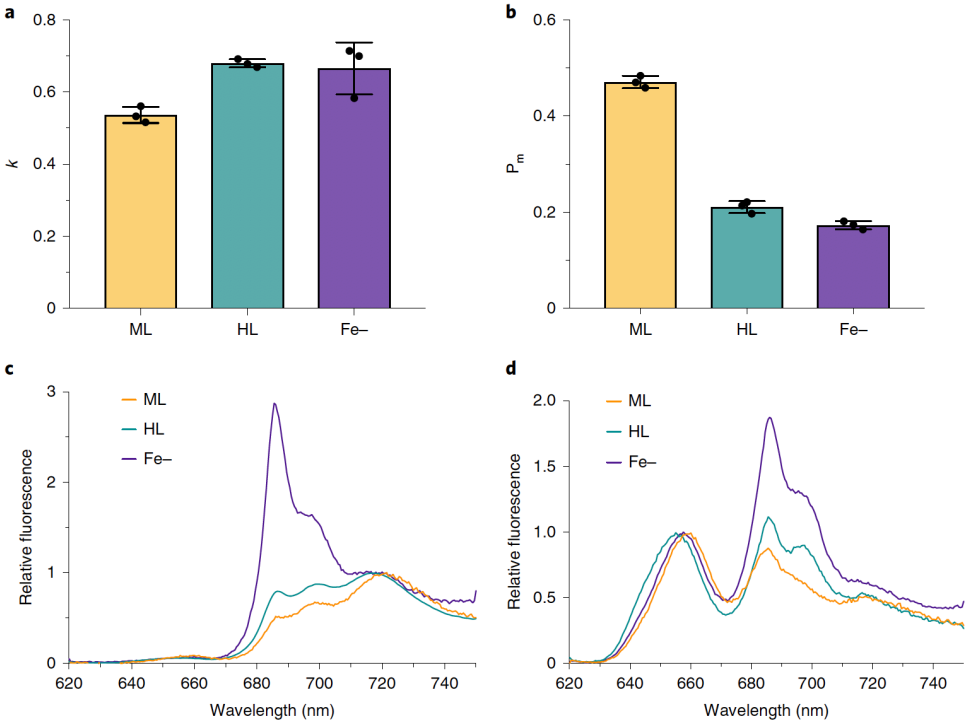

Fig. 5 | Functional characterization of IsiA in Syn7942 cells under ML, HL and Fe–conditions. a, *k*-values of first-degree exponential function fitted to P700 oxidation kinetics after application of 620-nm saturating pulse (3 ms, 20 mmol photons m^{-2} s^{-1}). Samples were dark-acclimated before each measurement, and Chl *a* concentration was adjusted to 20 µg ml^{-1}. Values represent mean ±s.d., $n = 3$ biologically independent experiments. **b**, Maximal amount of oxidized P700 (P_m) indicating the functionality of PSI. Values represent mean ±s.d., $n = 3$ biologically independent experiments. **c**, Average 77K fluorescence emission spectra of cells at 435-nm excitation, $n = 5$ biologically independent experiments. **d**, Average 77K fluorescence emission spectra of cells at 600-nm excitation, $n = 5$ biologically independent experiments. **c**,**d**, Chl *a* concentration was adjusted to 10 µg ml^{-1} for measurement.

Supramolecular organisation of PSI, PSII and Cyt b_6f in thylakoid membranes

Despite that a majority of thylakoid membrane fragments expose their cytoplasmic surface to AFM probes, we also performed high-resolution AFM imaging on the lumen surface of cyanobacterial thylakoids, as indicated by the absence of PSI cytoplasmic protrusions and the presence of PSI lumenal features (Fig. 6). Dimeric protrusions were the predominant features identified in the lumen surface of ML-adapted thylakoid membranes (Fig. 6a, 6b). These dimers could be divided into two groups, one of which has a larger peak-to-peak distance of protrusions (8.9 ± 0.9 nm, n = 15) than the other with reduced distance between peaks (6.2 ± 0.7 nm, n = 15) (Fig. 6c), reminiscent of PSII (PDB: 3WU2) and Cyt b_6f (PDB: 2E74) dimers, respectively

(Fig. 6d). Therefore, the dimers with a larger separation of protrusions were assigned to be PSII dimers and the dimers with a smaller separation of protrusions were assigned to be Cyt b_6f dimers. During AFM tip scanning, PSII protrusions above the thylakoid lumen surface were more stable than the PSI protrusions on the cytoplasmic surface (Supplementary Fig. 10), suggesting the relatively strong interactions between the PSII core and extrinsic PsbO, PsbP, PsbQ, PsbU, and PsbV subunits.

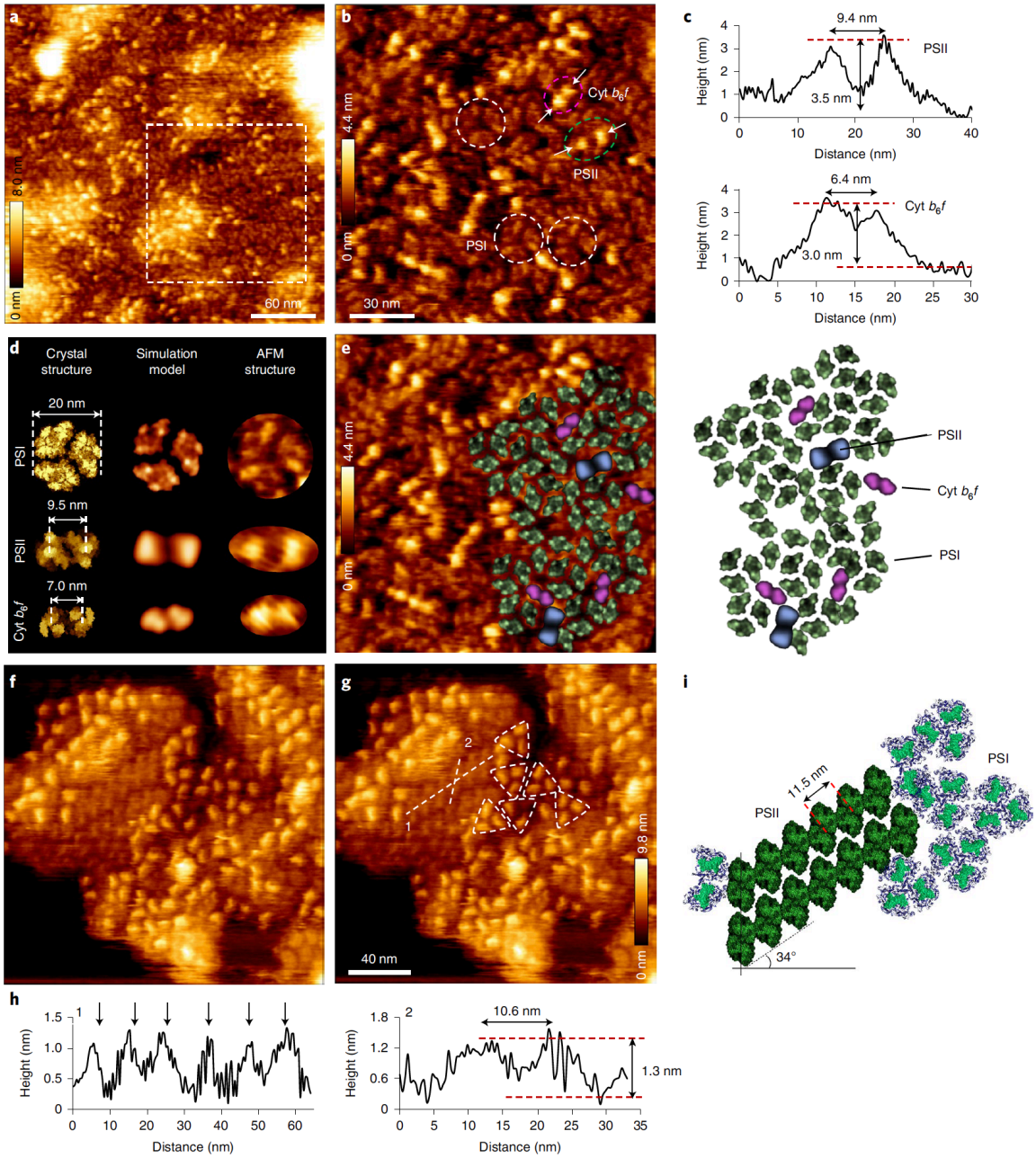

Fig. 6 | AFM images reveal PSII and Cyt b_6f in thylakoid membranes from ML-adapted Syn7942. a, High-resolution AFM image of the luminal surface of thylakoid membranes, showing the densely packed photosynthetic membrane proteins. The area represented by the white box is shown in **b**. **b**, Zoomed-in view of the area highlighted in **a**. PSI trimers are highlighted with white dashed circles based on their unique topography as shown in **d**. Putative PSII and Cyt b_6f complexes are highlighted by a green and pink oval, respectively, based on the distance between their two monomers from the luminal membrane surface. White arrows indicate the positions of height profiles. **c**, Height profiles corresponding to PSII and Cyt b_6f in **b**. The lateral distance between peaks of PSII is 8.9 ± 0.9 nm, $n = 15$, and the height of protrusions from the membrane surface is 3.5 nm. The lateral distance between peaks of Cyt b_6f is 6.2 ± 0.7 nm, $n = 15$, and the height of protrusions from the membrane surface is 3.0 nm. **d**, Atomic structure (left), simulated AFM images based on PDB (middle) and AFM topograph (right) of PSI, PSII and Cyt b_6f from the luminal surface (PDB, PSI: 1JB0; PSII: 3WU2; Cyt b_6f: 2E74). The lateral size of PSI crystal structure and distances of protrusions in the PSII and Cyt b_6f crystal structures are shown. **e**, Model of the arrangement of PSI, PSII and Cyt b_6f within the thylakoid membrane, constructed with simulated AFM images of PSI (green), PSII (blue) and Cyt b_6f (purple). **f**, High-resolution AFM image of the cytoplasmic surface of thylakoid membrane showing the ordered array of dimeric complexes that are speculated to be PSII dimers. **g**, Same image as **f**, with PSI trimers highlighted by triangles and positions of height profiles shown as dashed lines. **h**, Height profiles corresponding to the dashed lines in **g**. Black arrows denote the peaks of profile 1. The lateral distance between the peaks of profile 2 is 10.6 nm, and the height of protrusions from the membrane surface is 1.3 nm. **i**, Structural model of the arrangement of PSII dimers in ordered array and PSI trimers. The space between adjacent PSII dimers is 11.5 nm, and the tilt angle of PSII array is 34°. Representative AFM imaging was derived from at least three biologically independent membrane preparations.

The lumenal structure of PSI complexes (Fig. 6b, circles) exhibits no significant protrusions in contrast to PSII and Cyt b_6f lumen sides. The PSI trimer has a diameter of 19.0 nm, consistent with the PSI crystal structure (PDB: 1JB0)[30] (Fig. 6d). PSII and Cyt b_6f dimers are interspersed with PSI complexes and the local contacts between individual membrane complexes ensure the formation of PSII−Cyt b_6f−PSI clusters to facilitate photosynthetic linear electron flow (Fig. 6e). There are various binding patterns of PSI and Cyt b_6f complexes (Supplementary Fig. 11), suggesting that the contacting domains of the two membrane complexes are flexible. Variable orientations of PSI and Cyt b_6f have also been reported in the isolated PSI−Cyt b_6f complexes from *Arabidopsis*[35]. By contrast, only one form of PSI−Cyt b_6f association was reported in *Chlamydomonas*[36].

In some membrane regions, parallel arrays of PSII dimers were visualised from the cytoplasmic surface (Fig. 6f, 6g, Supplementary Fig. 12), reminiscent of cryo-electron tomography results[37]. The centre-to-centre distance between two coupled dimers within the same row is 11.1 ± 0.7 nm (n = 5) (Fig. 6h), consistent with the space between PSII dimers in the crystal lattice (11.6 nm)[38]. The distance between the two protrusions of the dimeric structure is 10.6 nm and the vertical protrusion from the membrane surface is 1.3 nm (Fig. 6h), in good agreement with the dimension of PSII dimers at the cytoplasmic side (PDB: 3WU2)[39]. It is generally considered that the phycobilisome cores dock predominately on the cytoplasmic surface of PSII[40]. The crystallised arrays of PSII dimers indicate that the phycobilisomes that tightly bind with these PSII dimers form arrays on the thylakoid surface. The angle between the extension of PSII arrays and the direction perpendicular to PSII dimer long axis is 34° (Fig. 6i), important for docking of phycobilisomes to PSII to form phycobilisome arrays[41]. EM images of the isolated phycobilisome-attached thylakoid membranes showed the ordered arrays of phycobilisomes on thylakoid membranes (Supplementary Fig. 12a-12d), similar to the observations of Syn6803 cells[37]. The less-ordered arrangement of phycobilisomes on thylakoid surface was also discerned (Supplementary Fig. 12c, 12d), suggesting the disordered PSII organisation (Fig. 6e).

The PSI trimers and dimers around the rows of PSII dimers have close contacts with PSII dimers, implying the possibility of PSII−PSI supercomplex formation in native thylakoid membranes (Fig. 6g, 6i). Based on the AFM topographs, we proposed the structural models of PSI and PSII associations in the local thylakoid membrane environment to elucidate the potential interactions of phycobilisomes with PSI and PSII (Supplementary Fig. 13). One model shows a PSII dimer closely associated with several PSI complexes (Supplementary Fig. 13a, 13b), and the other displays a PSII dimer array surrounded by PSI complexes (Supplementary Fig. 13c, 13d). Docking of phycobilisomes on the photosynthetic complex clusters indicates the possible organisation of phycobilisome-PSII-PSI megacomplexes[22], shedding light on the regulatory mechanism of state transitions. Within the phycobilisome-PSII-PSI megacomplex, for example in Syn6803, excitation energy captured by the phycobilisome is transferred from the allophycocyanin core to PSII through the terminal emitter ApcE, or to PSI through the terminal emitter ApcD[40,42]. Control of energy transfer could be accomplished by the local conformational changes of photosynthetic complexes. The close contacts between PSII and PSI complexes may also provide a means for the "spillover" of excitation energy from PSII to PSI. The dynamic organisations of photosynthetic complexes and the regulatory mechanisms of state transition remain to be further investigated.

ATPase-like structures

AFM visualised many ring-like structures in the ML-, HL- and Fe- adapted thylakoid membranes (Fig. 1, 7a, Supplementary Fig. 4, 6, 8). These ring structures had no specific distribution patterns in thylakoid membranes and no defined binding with adjacent IsiA−PSI complexes (Fig. 7b). The outer diameter and the peak-to-peak diameter of the ring-like structure were 7.37 ± 0.24 nm (n = 31) and 4.6 ± 0.2 nm (n = 24), respectively, and the protrusion of the ring structure from the cytoplasmic thylakoid surface was 1.2 ± 0.2 nm (n = 15), which was 0.41 ± 0.25 nm (n = 15) higher than IsiA (Fig. 7c, 7d). These features are consistent with the dimensions of the C_{14} ring of ATPase[43,44]. Likewise, 14-fold symmetrised correlation average AFM topograph of the ring structure (Fig. 7e) resembles the cryo-EM structure and AFM topographs of isolated ATPase complexes from chloroplasts[43,44] and cyanobacteria[45]. Based on these features, the ring structures were tentatively assigned to be the F_0 domain of ATPase in Syn7942. It is possible that the F_1 heads of ATPases that have a high protrusion from the membrane surface were swept away by AFM probes, as the immunoblot analysis confirmed the presence of the F_1 domain in the isolated thylakoid membranes used for AFM imaging (Supplementary Fig. 2c).

In mitochondria, the dimerisation of ATPases was thought to induce the local membrane curvature[46]. We found that ATPases in cyanobacterial thylakoid membranes are predominantly monomers (Supplementary Fig. 14), consistent with the ATPases in plant thylakoids[47]. Two tightly contacted ATPases were occasionally discerned close to slightly curved membrane regions (Fig. 7b, black arrows). The ATPase complexes could

interact tightly with PSI complexes (Fig. 1c, arrows). In the HL-adapted and Fe- adapted thylakoid membranes, ATPases could either associate with PSI complexes directly (Fig. 7b) or bind to IsiA assemblies of the IsiA–PSI supercomplex (Fig. 1g, 7c, Supplementary Fig. 15, 16), indicating the structural and functional links between ATPases and PSI, as well as the flexible binding of ATPases with PSI and IsiA.

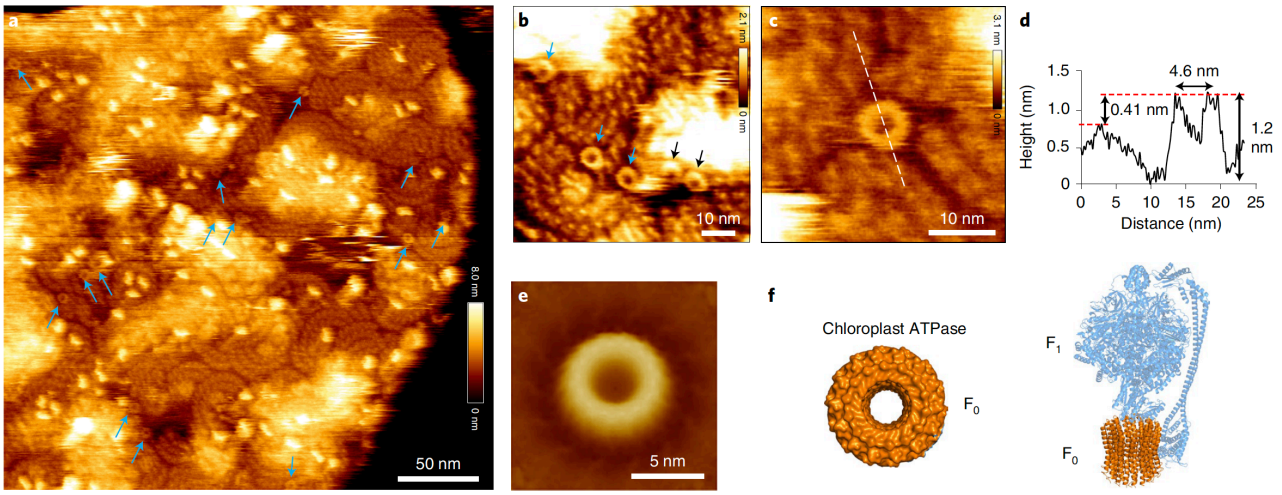

Fig. 7 | AFM images of putative ATPases in thylakoid membranes. a, High-resolution AFM image of the cytoplasmic surface of thylakoid membranes. The speculated ATPase rings are indicated by blue arrows. **b**, High-resolution AFM image showing the rings more clearly. Blue arrows indicate the dispersive individual rings and black arrows the neighbouring rings. **c**, Zoomed-in view showing the ring structure in more detail. Dashed line shows the position of the height profile. **d**, Height profiles corresponding to the dashed lines in **c**, with lateral distances and height differences shown. **e**, 14-fold symmetrized correlation-averaged AFM topograph of the ring structure. **f**, Atomic structure of the chloroplast ATPase (PDB: 6FKF). Left: top view of membrane domain F_0; right: front view of ATPase. Representative AFM imaging was derived from at least three biologically independent membrane preparations.

PSI–NDH-1 supercomplexes

We also observed another type of membrane supercomplexes in proximity to PSI complexes in thylakoid membranes (Fig. 8a, Supplementary Fig. 16). On the cytoplasmic surface, the supercomplex consists of a highly protruding domain in one end and four small protrusions in the other end (Fig. 8b, blue arrows), reminiscent of the structure of cyanobacterial NDH-1 complexes[48,49]. The four membrane domains possess a higher protrusion than IsiA proteins (0.4 nm) and are aligned in a line (Fig. 8c), making these structures distinguishable from IsiA assemblies. The spaces between the four lower-protruding domains are 6.0 nm, 3.7 nm, and 3.6 nm, respectively (Fig. 8c), in agreement with the cryo-EM structure of NDH-1 membrane domains (PDB: 6HUM)[48] (Fig. 8d). The overall AFM topograph of the multi-domain complex is highly consistent with the simulated structure based on the cyanobacterial NDH-1 cryo-EM results (Fig. 8e). Thus, these macromolecular structures were assigned as the NDH-1 complexes.

The height of the strongly protruded domains varies from 1 nm to 5 nm (Fig. 8c, 8g), consistent with the height of the hydrophilic arm of cyanobacterial NDH-1, which comprises NdhH, I, J, M, N, O, and S subunits[48,49]. Some NDH-1 structures have two protruding domains, a larger one that was assigned to be the hydrophilic arm and a smaller one that appears as the Cup domain including CupA, CupB, and CupS subunits[50-53] (Fig. 8f, 8g), resembling the NDH-1MS structure (PDB: 6TJV)[54]. Time-lapse AFM images showed the independent removal of the two protrusions (Fig. 8f-8h), eventually resulting in the exposure of NDH-1 membrane domains to AFM probes. AFM images allowed us to draw a model of the local organisation of IsiA–PSI, IsiA-only assemblies, NDH-1, and ATPases in cyanobacterial thylakoid membranes (Fig. 8i), which may function as a bioenergetic entity to fulfil and optimise photosynthetic linear and cyclic electron flow for ATP and NADPH production.

Based on the AFM image, a structural model of the IsiA–PSI–NDH-1 supercomplex is proposed to illustrate the possible electron flow within the photosynthetic supercomplex (Supplementary Fig. 17). Flavodoxin (Fld) or ferredoxin (Fd) accepts electrons from the PsaC subunit of PSI, and Fd binds to the peripheral domain of the NDH-1 hydrophilic arm transferring electrons to plastoquinone (PQ) to produce PQH_2[85,86]. The cyclic electron flow is completed by the transfer of electrons from PQ back to PSI via Cyt b_6f and plastocyanin. The formation of PSI–NDH-1 supercomplexes facilitates cyclic electron flux and is essential for balancing the ATP/NADPH ratio required for the Calvin–Benson cycle.

NDH-1 complexes were observed by AFM in both the HL- and ML-adapted thylakoid membranes (Supplementary Fig. 16, 18). In the HL-adapted thylakoid membranes, more NDH-1 complexes were detected (Supplementary Table 1), as HL could induce expression of NDH-1[27]. In the ML-adapted thylakoid membranes,

NDH-1 contacts directly with PSI forming the PSI–NDH-1 supercomplex (Supplementary Fig. 18) to maintain efficient cyclic electron transport, as suggested in plants and Syn6803[35,55-57]. NDH-1 could bind with PSI complexes or interact with the peripheral IsiA layers of the IsiA–PSI supercomplexes in diverse manners (Supplementary Fig. 16), indicating the variable, intricate association of NDH-1 with PSI and IsiA complexes.

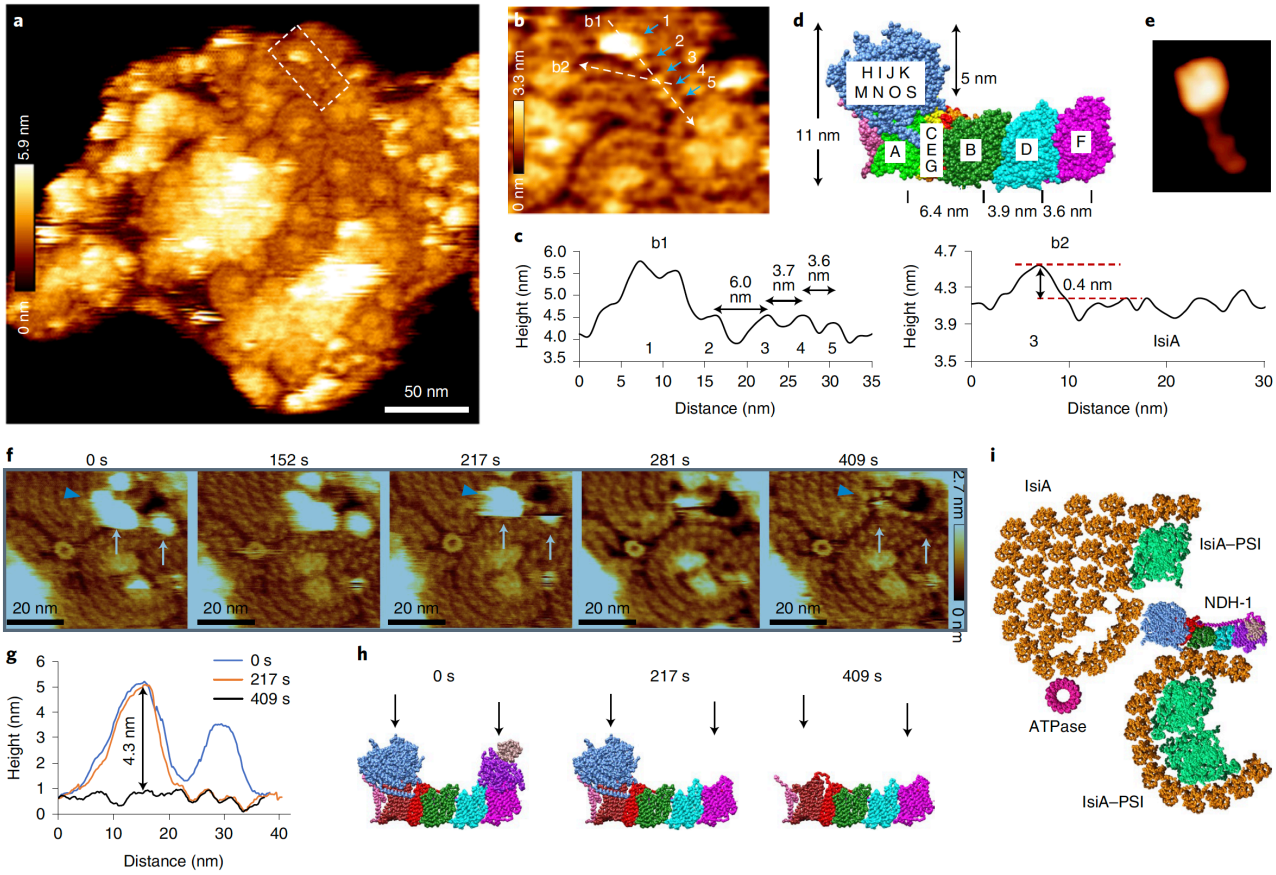

Fig. 8 | AFM images of putative NDH-1 in thylakoid membranes. a, High-resolution AFM image of the cytoplasmic surface of thylakoid membranes. The speculative NDH-1 complex is highlighted by the white box. **b**, Zoomed-in view of the area highlighted in **a** showing the speculative NDH-1 complex in more detail. Dashed lines show the positions of height profiles and blue arrows indicate protrusions of the DH-1 complex. **c**, Height profiles corresponding to the dashed lines in **b**, with lateral distances and height differences shown. **d**, Front view of the atomic structure of NDH-1 complexes (PDB: 6HUM). The height is 11 nm, and the height above the membrane domain is 5 nm. Distances between protrusions of the four membrane domains are 6.4, 3.9 and 3.6 nm, respectively. **e**, Simulated AFM images based on the cryo-EM structure (PDB: 6HUM). **f**, Time-lapse AFM imaging of the NDH-1 complex, revealing the removal of protruding subunits (white arrows); blue arrowheads show the position and direction of height profiles. **g**, Height profiles of NDH-1 complex corresponding to blue arrowheads in **f**. The height of the protrusion above the membrane domain is 4.3 nm. **h**, Nanodissection of speculated NDH-1 complex in **f** is modelled with NDH-1 atomic structure (PDB: 6TJV). Black arrows indicate the absent domains, as shown in **f** with white arrows. **i**, Structural model of the arrangement of IsiA–PSI, NDH-1 complex and ATPase. Representative AFM imaging was derived from at least three biologically independent membrane preparations.

Discussion

The cyanobacterial thylakoid membrane provides the natural platform to functionally position and regulate photosynthetic and respiratory protein complexes for efficient energy transfer and dynamic adaption to cope with environmental changes. *In vivo* expression of IsiA has been reported to be regulated by environmental stress factors and different growth stages[6-10,58]. Previous structural studies have focused on the IsiA–PSI complexes induced by iron-deficient conditions[6,7,11,12,15,31,59-62]. HL-induced expression of IsiA has been reported[9], but prior to this study, there was no structural analysis of the IsiA–PSI complexes generated under HL. Unlike the relatively homogeneous IsiA–PSI structures revealed by single-particle EM[6,7,11,12], AFM images revealed the structural variability of IsiA–PSI supercomplexes in the native cyanobacterial thylakoid membranes. PSI trimers, dimers, or monomers could be associated with a single, double, triple, or multiple IsiA rings, indicative of the flexible interaction between IsiA and PSI (Fig. 3b, Supplementary Table 2). IsiA proteins can also self-aggregate to form IsiA-only assemblies in the PSI-rich regions (Fig. 3e, 4d). These observations suggest that the belt of IsiA proteins is unable to alter the aggregation states of PSI complexes. It is conceivable that the diverse IsiA–PSI complexes in native membranes represent structural intermediates generated at different growth conditions during the dynamic biogenesis process of IsiA–PSI supercomplexes and may have different photosynthetic functions. EM of isolated IsiA–PSI complexes so far has only reported

a single or double IsiA encircling PSI[6,7,11,12,15,31], suggesting that the extra IsiA rings may have relatively weaker interactions with the central IsiA−PSI complex. The flexible interaction and dynamic assembly were supported by the previous finding that IsiA proteins are mobile in cyanobacterial thylakoid membranes[63].

The exact function of IsiA in cyanobacteria has remained obscure. There are three prevalent hypotheses for IsiA functions: (1) store the majority of chlorophylls to compensate for the loss of photosystems[17,64]; (2) serve as an accessory antenna for PSI to increase the light cross-section of PSI[6,7,12,14,33,65]; (3) dissipate excess excitation energy for photoprotection[9,16,66]. Our spectroscopic results indicated that IsiA could function as an alternative light-harvesting antenna funnelling energy to PSI under stress conditions (Fig. 5), consistent with the *in vitro* results[12], and the tight association of IsiA and PSI complexes increase the absorption cross-section and antenna size per PSI. The upregulation of IsiA and formation of IsiA−PSI supercomplexes could thus compensate for the great loss of phycobilisomes and PSI induced by HL and iron stress (Supplementary Fig. 1, 2). As cells grow faster in HL, they may encounter iron limitations, such as the rate of Fe uptake for production of PSI reaction centres. Substituting IsiA for PSI could be a general adaptive mechanism to rapid growth, resulting in the reduced demand for Fe and allowing cyanobacteria to survive in diverse environmental conditions. Moreover, the highly fluorescent, functionally-decoupled IsiA, probably the peripheral IsiA rings within the IsiA−PSI supercomplexes and IsiA-only assemblies as observed in AFM (Fig. 3, Supplementary Figs. 5,7,8), might act as a Chl store when losing photosystems in physiological regulation, which merits further explorations.

The phycobilisomes represent membrane-associated light-harvesting antenna in cyanobacteria and red algae[67-69]. Apart from the light-harvesting function, phycobilisomes also contribute to nitrogen storage and photoprotection to cope with environmental stress[70,71]. During the evolution of photosynthetic organisms, phycobilisomes were gradually replaced by membrane-spanning Chl-containing antenna including IsiA and homologs, signifying the varying stress-response mechanisms of photosynthetic apparatus to enable their hosting organisms to adapt to the living niches[72].

AFM topographs outline the native organisation of photosynthetic apparatus at the long-range scale and local membrane domains. At the sub-micron scale, photosynthetic membrane complexes have the propensity to segregate and form functional domains throughout the Syn7942 thylakoid membranes, such as PSI-enriched regions (Figs. 1-3) and PSII arrays (Fig. 6f, Supplementary Fig. 12), consistent with fluorescence microscopic observations from Syn7942[19] and Syn6803[73] cells. Given the differences between PSI and PSII in their absorption and turnover rates, the lateral segregation of photosystems in thylakoid membranes may provide favourable micro-environments for photosynthetic linear electron flow[18]. In the PSI-enriched membrane regions of Syn7942, PSI trimers display relatively random orientation, reminiscent of our previous study[19] and the PSI organisation in Syn6803[20]. By contrast, PSI trimers in the thylakoid membranes of *Thermosynechococcus elongatus* and *Synechococcus* sp. PCC 7002 are closely packed to form regular lattices[20]. Moreover, previous EM studies have reported the presence of crystalline PSII arrays in thylakoid membranes from Syn6803 after mild detergent solubilisation[74]. To our knowledge, the present study provides the first view of multiple rows of PSII dimers surrounded by PSI complexes in native cyanobacterial thylakoid membranes, without detergent treatment (Fig. 6, Supplementary Fig. 12). The specific PSII organisation is speculated to facilitate the association of phycobilisomes[69,75]. The respiratory NDH-1 and succinate dehydrogenase complexes have also been reported to be clustered in thylakoid membranes to favour respiratory electron flow towards terminal oxidases[27]. Our finding corroborates that the structural heterogeneity and compartmentalisation of bioenergetic membranes are prevalent in prokaryotes and eukaryotes[76-80], providing the structural basis for high-efficiency metabolism and regulation.

There is increasing experimental evidence unveiling the formation of supercomplexes in cyanobacterial [21,22,57,81]and chloroplast thylakoids[55,56,82,83], as well as mitochondria[84]. AFM imaging on native membranes permits the visualisation of membrane supercomplexes formed by weak or flexible interactions. We showed that in the Syn7942 thylakoid membranes, some PSI complexes contact directly with PSII, Cyt b_6f, ATPase, and NDH-1. The association of PSI, Cyt b_6f, and PSII dimer arrays (Fig. 6, Supplementary Fig. 13) facilitates photosynthetic linear electron flow and the balance of excitation energy transfer from phycobilisomes to PSII or PSI. Consistently, recent studies have suggested the presence of PSII−PSI supercomplexes[21] and the PSII−PSI−phycobilisome megacomplexes[22] from Syn6803. Intermixing of PSII and Cyt b_6f complexes could facilitate exchange of plastoquinol/plastoquinone molecules, thereby efficient electron transport from PSII to Cyt b_6f. ATPases also appear in proximity to PSI, indicative of their structural and functional associations.

Our AFM topographs also provide the structural evidence of PSI−NDH-1 supercomplexes in thylakoid membranes (Fig. 8, Supplementary Fig. 16-18) and allow us to propose a structural model of PSI−NDH-1 supercomplexes to elucidate cyclic electron flow (Supplementary Fig. 17). The close associations between PSI and NDH-1 could abridge the electron transport pathway and increase the rate of cyclic electron transport to

balance the cellular ATP/NADPH ratio in cyanobacteria and plants[5755,56,83]. AFM images also revealed diverse forms of PSI−NDH-1 supercomplexes that vary in the binding sites between PSI, IsiA−PSI, and NDH-1 as well as the oligomeric states of PSI (Fig. 8, Supplementary Fig. 16-18), suggesting that the associations between PSI and NDH-1 are highly flexible and dynamic. This observation is supported by the previous finding that the reorganisation of NDH-1 in cyanobacterial thylakoid membranes, through associating with PSI or forming respiratory clusters under different light regimes, may function as a biological "switch" to regulate the prevalence of linear and cyclic electron flow[27].

In summary, by applying high-resolution AFM imaging at the near-physiological conditions and biochemical and spectroscopic analysis, we obtain a molecule-level view of the native architecture of cyanobacterial thylakoid membranes. We find that (1) both HL and Fe- could induce expression of IsiA in Syn7942 and the constructed IsiA−PSI supercomplexes possess diverse configurations in thylakoid membranes; (2) IsiA proteins act as an alternative light-harvesting antenna to increase the effective absorption cross-section of PSI; (3) cyanobacterial thylakoid membranes are laterally heterogeneous and compartmentalise electron transport membrane complexes; (3) direct associations of PSI−PSII, PSI−Cyt b_6f, PSI−ATPase, and PSI−NDH-1 indicate their functional coordination and propensity to form bioenergetic supercomplexes. Viewing the structural landscape of cyanobacterial thylakoid membranes highlights the building and regulatory principles of functional photosynthetic apparatus, and will inform bioengineering to enhance photosynthetic performance and bioenergy production. Knowledge of the photosynthetic membrane organisation could be extended to other bacterial membrane systems, as well as chloroplast thylakoid and mitochondrial membranes.

Methods

Strains and growth conditions, generation of mutants

Synechococcus elongatus PCC7942 (Syn7942) was cultivated in Multi-Cultivator MC 1000-OD (Photon Systems Instruments) with BG11 or iron-free BG11 medium at 30°C. The culture was bubbled with air and illuminated with constant cool white LEDs (Moderate light (ML): 40 μmol photons·m^{-2}·s^{-1}; high light (HL): 300 μmol photons·m^{-2}·s^{-1})[27-29]. Iron-free BG11 was prepared as described[87]. Iron-deficiency treatment of cells was performed as reported previously[88] with a slight modification. Cells from the mid-logarithmic growth phase iron-replete cultures were pelleted at room temperature, resuspended, and washed sequentially four times with iron-free BG11. The cultures were then resuspended in iron-free BG-11 to OD_{750} = 0.2 and grown under ML.

The *isiA* gene (Synpcc7942_1542) was deleted by replacing the *isiA* gene with spectinomycin resistance cassette following the Redirect strategy[89] based on homologous recombination[90]. Primers used in this work were listed in Supplementary Table 3. To grow the mutant cells, BG-11 medium was supplemented with spectinomycin at 25 μg·mL^{-1}. Segregation of the mutation was confirmed by PCR (Supplementary Fig. 9).

Absorption spectra

Whole-cell absorption spectra were measured at room temperature using a Cary UV-Vis Spectrophotometer (Agilent Technologies). The OD_{750} of cells was adjusted to 0.5 before measurement. Absorption spectra of isolated thylakoid membranes were normalised by the absorption peak at 682 nm.

Thylakoid membrane isolation

Syn7942 cells were pelleted by centrifugation and washed with buffer A (50 mM MES-NaOH, pH 6.5, 5 mM $CaCl_2$, and 10 mM $MgCl_2$)[91]. Cell pellets were resuspended in buffer A containing 25% glycerol and broken by glass bead (212–300 μm in diameter) at 4°C. Phycobilisomes were decoupled from the thylakoid membranes and disassembled in buffer A (Supplementary Fig. 12a, 12b). Crude thylakoid membrane fractions were isolated as described previously[19,92]. To obtain pure thylakoid membranes for AFM imaging, further separation of the membrane fractions was performed in a step sucrose gradient (2.0 M, 1.3 M, 1.0 M, 0.5 M) and centrifuged at 36,200 rpm in Beckman RPS40 rotor for 1 h at 4°C. The Chl-enriched samples at the 1.0-1.3 M sucrose interface were collected and characterised by high-resolution AFM imaging in buffer. No detergent was added during membrane isolation and AFM imaging to ensure the physiological organisation of isolated thylakoid membranes.

Phycobilisome-associated thylakoid membranes were isolated following the previous procedure[69,75] with slight modifications. Syn7942 cells were pelleted by centrifugation, washed with buffer PC (0.5 M potassium phosphate, 0.3 M sodium citrate), and resuspended in buffer SPC (0.5 M sucrose, 0.5 M potassium

phosphate, 0.3 M sodium citrate). Phycobilisome-thylakoid membrane fractions were isolated using a step sucrose gradient. The samples at the 1.0-1.3 M sucrose interface were collected for EM imaging.

Atomic force microscopy (AFM)
Two microliters of thylakoid membrane samples were adsorbed onto freshly cleaved mica surface with 38 µL of adsorption buffer (10 mM Tris–HCl, pH 7.5, 150 mM KCl, 25 mM $MgCl_2$) at room temperature for 1.5 h. After adsorption, the sample was carefully rinsed with 800 µL imaging buffer (10 mM Tris–HCl, pH 7.5, 150 mM KCl)[71]. High-resolution imaging was performed in AC imaging mode in liquid at room temperature using a NanoWizard 3 AFM (JPK) equipped with an ULTRA S scanner and Ultra-Short Cantilever probe (0.3 $N \cdot m^{-1}$, Nano World) at scan frequencies of 5 Hz using optimised feedback parameters and a resolution of 512 × 512 pixels. The tip spring constant was routinely calibrated. Images were processed with JPK SPM Data Processing (JPK) and ImageJ.

Simulation of AFM images
Chimera, ImageJ, and WSxM were used to simulate AFM images of the PSI, PSII, Cyt b_6f, NDH-1 complexes and IsiA−PSI supercomplex. The simulation was carried out with sphere models of atomic structures of each complex generated by using the Chimera package[93]. Tagged image file format (TIFF) file of the sphere model was scaled at X and Y dimension and calibrated at Z dimension according to the size of atomic structure by using ImageJ, and imported as text image file. Text file was processed by using the tip-surface dilation option with the tip radius of 0.5 nm in WSxM. The simulated AFM image was then smoothed by Gaussian smooth with a decay distance 20, and the structure above the thylakoid membrane surface was shown by adjusting the Z scale.

SDS-polyacrylamide gel electrophoresis (SDS-PAGE), blue native-PAGE, and immunoblot analysis
For denatured electrophoresis, crude thylakoid membrane proteins were denatured as described[13] and were separated by 15% (w/v) SDS-PAGE. For native gel electrophoresis, thylakoid membrane proteins were studied by blue native-PAGE as previously reported[94] with the exception that 3 % DM was used for solubilisation. Precast gradient polyacrylamide gels from 4 to 16% (NativePAGE™, Thermo Fisher) were used to separate protein complexes in their native forms. After electrophoresis, proteins were transferred to a PVDF membrane (Immobilon-P, Millipore) and analysed with the antibodies specific to IsiA (ImmunoGen Biological Technology Co., Ltd), PsaB, PsbA (D1) and ATPase (Agrisera).

P700 oxidation kinetics
P700 oxidation kinetics of intact cells was recorded using a pulse amplitude modulated fluorometer Dual-PAM-100 (Walz, Germany). Before measurements, cell suspensions at the Chl concentration of 20 $\mu g \cdot mL^{-1}$ were dark-acclimated. To measure the PSI absorption cross-section, P700 was oxidised by a saturating 3 ms 620 nm LED light pulse (20 mmol photons$\cdot m^{-2} \cdot s^{-1}$). The oxidation phase was then fitted with 1st-degree exponential function to obtain *k*-value. The maximal change in the P700 signal (P_m) upon transformation of P700 from fully reduced to fully oxidised states was achieved by applying a saturation pulse (5000 µm photons$\cdot m^{-2} \cdot s^{-1}$) on the strong far red (720 nm, 75 $W \cdot m^{-2}$) background illumination. Five independent cultures were measured.

77K fluorescence spectra
The 77K fluorescence emission spectra of intact cells were measured using a Perkin-Elmer LS50 luminescence spectrometer (Foster City, CA) equipped with a liquid-nitrogen sample housing and a red-sensitive photomultiplier. The Chl concentration of the samples was adjusted to 10 $\mu g \cdot mL^{-1}$. Samples frozen in liquid nitrogen were excited with the 435 nm or 600 nm light. Fluorescence emission was recorded in the range of 620-750 nm. The excitation and emission slit widths were 5 nm. Five independent cultures were measured.

Mass spectrometry
Isolated thylakoid membranes were washed with PBS buffer and were treated as previously described[95]. 50 µg of isolated thylakoid membrane proteins were reconstituted in 25mM ambic and 1% (w/v) Rapigest SF (Waters, UK). Samples were reduced by the addition of 5 mM dithiothreitol (DTT). Protein alkylation was carried out by addition of 10 mM iodoacteamide (IAM) and incubation at RT for 30min in the dark. Excess IAM was quenched by addition of 5 mM DDT. Digestion with trypsin (1:100 trypsin:protein ratio, Promega Gold) was carried overnight at 37°C. Rapigest was then removed by addition of 0.5% (v/v) TFA. Digests were centrifuged at 17,200 g for 30min and the clarified supernatants aspirated. Samples were stage–tipped on C18 filters to

remove Chls prior to LC-MSMS analysis. Data-dependent LC-MS/MS analysis was conducted on a QExactive quadrupole-Orbitrap mass spectrometer coupled to a Dionex Ultimate 3000 RSLC nano-liquid chromatograph (Hemel Hempstead, UK). The raw data file was imported into Progenesis QI for Proteomics (Version 3.0 Nonlinear Dynamics, Newcastle upon Tyne, UK, Waters Company). Peak picking parameters were applied with the sensitivity set to maximum and features with charges of 2^+ to 7^+ were retained. A Mascot Generic File, created by Progenesis, was searched against the *Synechococcus elongatus* database from UniProt.

Electron microscopy
Isolated phycobilisome-thylakoid membranes were characterised using negative staining transmission electron microscope (TEM). The samples were stained with 3% uranyl acetate. Images were recorded using an FEI Tecnai G2 Spirit BioTWIN transmission electron microscope equipped with a Gatan Rio 16 camera.

Data availability
The source data underlying Figs. 1c, 2e, 2f, 4a-4d, 5, 6c, 6h, 6d, 7d, 8c, 8g and Supplementary Figs. 1b, 1c, 2a-2c, 4b, 4d, 9b, 9d, 12b, 14b and Supplementary Table 1, 2 are provided as a Source Data file. All data are available from the corresponding author upon request.

Correspondence and requests for materials should be addressed to L.-N.L. or Y.-Z.Z.

Acknowledgements
We thank Dr. Jorge Rodriguez-Ramos for the support of AFM data analysis and Ms Fang Zhao for data analysis. We thank the Liverpool Centre for Cell Imaging and Centre for Proteome Research for technical assistance and provision. We also thank Gregory F. Dykes and Alison Beckett for electron microscopy technical support. This work was supported by the Royal Society University Research Fellowship (UF120411 and URF\R\180030, L.-N.L.), Royal Society Grants (RGF\EA\181061, RGF\EA\180233, IEC\NSFC\191600, L.-N.L.), Biotechnology and Biological Sciences Research Council Grant (BB/R003890/1, BB/M024202/1, BB/M012441/1, L.-N.L.), the Queen Mary Principal's research studentship (S.W.), the National Science Foundation of China (31630012, U1706207, 91851205, Y.-Z.Z.), the National Key R & D Program of China (2018YFC1406700, Y.-Z.Z.), Major Scientific and Technological Innovation Project (MSTIP) of Shandong Province (2019JZZY010817, Y.-Z.Z.), the AoShan Talents Cultivation Program supported by Pilot National Laboratory for Marine Science and Technology (Qingdao), China (2017ASTCP-OS14, Y.-Z.Z.), Taishan Scholars Program of Shandong Province, China (tspd20181203, Y.-Z.Z.), the National Natural Science Foundation of China grants (31770128 and 91851103, Q.W.) and China Postdoctoral Science Foundation Funded Project (2019M662335, L.-S.Z).

Author contributions
L.-S.Z., Y.-Z.Z. and L.-N.L. conceived the project; L.-S.Z., T.H., S.W., D.M.S., C.W.M., and L.-N.L. performed the research; L.-S.Z., T.H. S.W., D.M.S., Q.W., A.V.R., C.W.M., Y.-Z.Z. and L.-N.L. analysed the data; L.-S.Z., T.H., C.W.M., Y.-Z.Z. and L.-N.L. wrote the manuscript. All of the authors discussed and commented on the results and the manuscript.

Competing interests
The authors declare no conflict of interests.

References
1 Liu, L. N. Distribution and dynamics of electron transport complexes in cyanobacterial thylakoid membranes. *Biochim Biophys Acta* **1857**, 256-265, doi:10.1016/j.bbabio.2015.11.010 (2016).
2 Vermaas, W. F. in *Encyclopedia of Life Sciences* 245-251 (Nature Publishing Group, 2001).
3 Mullineaux, C. W. Co-existence of photosynthetic and respiratory activities in cyanobacterial thylakoid membranes. *Biochim Biophys Acta* **1837**, 503-511, doi:10.1016/j.bbabio.2013.11.017 (2014).
4 Saer, R. G. & Blankenship, R. E. Light harvesting in phototrophic bacteria: structure and function. *Biochem J* **474**, 2107-2131, doi:10.1042/Bcj20160753 (2017).
5 Chen, H.-Y. S., Bandyopadhyay, A. & Pakrasi, H. B. Function, regulation and distribution of IsiA, a membrane-bound chlorophyll a-antenna protein in cyanobacteria. *Photosynthetica* **56**, 322-333, doi:10.1007/s11099-018-0787-7 (2018).

6 Bibby, T. S., Nield, J. & Barber, J. Iron deficiency induces the formation of an antenna ring around trimeric photosystem I in cyanobacteria. *Nature* **412**, 743-745, doi:Doi 10.1038/35089098 (2001).
7 Boekema, E. J. *et al.* A giant chlorophyll-protein complex induced by iron deficiency in cyanobacteria. *Nature* **412**, 745-748, doi:10.1038/35089104 (2001).
8 Vinnemeier, J., Kunert, A. & Hagemann, M. Transcriptional analysis of the isiAB operon in salt-stressed cells of the cyanobacterium Synechocystis sp. PCC 6803. *Fems Microbiol Lett* **169**, 323-330, doi:Doi 10.1016/S0378-1097(98)00478-9 (1998).
9 Havaux, M. *et al.* The chlorophyll-binding protein IsiA is inducible by high light and protects the cyanobacterium Synechocystis PCC6803 from photooxidative stress. *FEBS Lett* **579**, 2289-2293, doi:10.1016/j.febslet.2005.03.021 (2005).
10 Yousef, N., Pistorius, E. K. & Michel, K. P. Comparative analysis of idiA and isiA transcription under iron starvation and oxidative stress in Synechococcus elongatus PCC 7942 wild-type and selected mutants. *Arch Microbiol* **180**, 471-483, doi:10.1007/s00203-003-0618-4 (2003).
11 Toporik, H., Li, J., Williams, D., Chiu, P. L. & Mazor, Y. The structure of the stress-induced photosystem I-IsiA antenna supercomplex. *Nat Struct Mol Biol* **26**, 443-449, doi:10.1038/s41594-019-0228-8 (2019).
12 Cao, P. *et al.* Structural basis for energy and electron transfer of the photosystem I-IsiA-flavodoxin supercomplex. *Nat Plants* **6**, 167-176, doi:10.1038/s41477-020-0593-7 (2020).
13 Ma, F. *et al.* Dynamic Changes of IsiA-Containing Complexes during Long-Term Iron Deficiency in Synechocystis sp PCC 6803. *Molecular Plant* **10**, 143-154, doi:10.1016/j.molp.2016.10.009 (2017).
14 Sun, J. L. & Golbeck, J. H. The Presence of the IsiA-PSI Supercomplex Leads to Enhanced Photosystem I Electron Throughput in Iron-Starved Cells of Synechococcus sp PCC 7002. *J Phys Chem B* **119**, 13549-13559, doi:10.1021/acs.jpcb.5b02176 (2015).
15 Chauhan, D. *et al.* A novel photosynthetic strategy for adaptation to low-iron aquatic environments. *Biochemistry* **50**, 686-692, doi:10.1021/bi1009425 (2011).
16 Park, Y. I., Sandstrom, S., Gustafsson, P. & Oquist, G. Expression of the isiA gene is essential for the survival of the cyanobacterium Synechococcus sp. PCC 7942 by protecting photosystem II from excess light under iron limitation. *Mol Microbiol* **32**, 123-129, doi:10.1046/j.1365-2958.1999.01332.x (1999).
17 Schoffman, H. & Keren, N. Function of the IsiA pigment-protein complex in vivo. *Photosynth Res*, doi:10.1007/s11120-019-00638-5 (2019).
18 Busch, K. B., Deckers-Hebestreit, G., Hanke, G. T. & Mulkidjanian, A. Y. Dynamics of bioenergetic microcompartments. *Biol Chem* **394**, 163-188, doi:10.1515/hsz-2012-0254 (2013).
19 Casella, S. *et al.* Dissecting the Native Architecture and Dynamics of Cyanobacterial Photosynthetic Machinery. *Mol Plant* **10**, 1434-1448, doi:10.1016/j.molp.2017.09.019 (2017).
20 MacGregor-Chatwin, C. *et al.* Lateral Segregation of Photosystem I in Cyanobacterial Thylakoids. *Plant Cell* **29**, 1119-1136, doi:10.1105/tpc.17.00071 (2017).
21 Bečková, M. *et al.* Association of Psb28 and Psb27 proteins with PSII-PSI supercomplexes upon exposure of *Synechocystis* sp. PCC 6803 to high light. *Mol Plant* **10**, 62-72, doi:10.1016/j.molp.2016.08.001 (2017).
22 Liu, H. *et al.* Phycobilisomes supply excitations to both photosystems in a megacomplex in cyanobacteria. *Science* **342**, 1104-1107, doi:10.1126/science.1242321 (2013).
23 Liu, L. N. & Scheuring, S. Investigation of photosynthetic membrane structure using atomic force microscopy. *Trends Plant Sci* **18**, 277-286, doi:10.1016/j.tplants.2013.03.001 (2013).
24 MacGregor-Chatwin, C. *et al.* Membrane organization of photosystem I complexes in the most abundant phototroph on Earth. *Nat Plants* **5**, 879-889, doi:10.1038/s41477-019-0475-z (2019).
25 Riediger, M. *et al.* Biocomputational Analyses and Experimental Validation Identify the Regulon Controlled by the Redox-Responsive Transcription Factor RpaB. *iScience* **15**, 316-331, doi:10.1016/j.isci.2019.04.033 (2019).
26 Kappell, A. D., Bhaya, D. & van Waasbergen, L. G. Negative control of the high light-inducible hliA gene and implications for the activities of the NblS sensor kinase in the cyanobacterium Synechococcus elongatus strain PCC 7942. *Arch Microbiol* **186**, 403-413, doi:10.1007/s00203-006-0154-0 (2006).
27 Liu, L. N. *et al.* Control of electron transport routes through redox-regulated redistribution of respiratory complexes. *Proc Natl Acad Sci U S A* **109**, 11431-11436, doi:10.1073/pnas.1120960109 (2012).
28 Sun, Y. *et al.* Light modulates the biosynthesis and organization of cyanobacterial carbon fixation machinery through photosynthetic electron flow. *Plant Physiol* **171**, 530-541, doi:10.1104/pp.16.00107 (2016).
29 Sun, Y., Wollman, A. J. M., Huang, F., Leake, M. C. & Liu, L. N. Single-organelle quantification reveals the stoichiometric and structural variability of carboxysomes dependent on the environment. *Plant Cell* **31**, 1648-1664 (2019).

30 Jordan, P. *et al.* Three-dimensional structure of cyanobacterial photosystem I at 2.5 A resolution. *Nature* **411**, 909-917, doi:10.1038/35082000 (2001).
31 Yeremenko, N. *et al.* Supramolecular organization and dual function of the IsiA chlorophyll-binding protein in cyanobacteria. *Biochemistry* **43**, 10308-10313, doi:10.1021/bi0487721 (2004).
32 Zipfel, W. & Owens, T. G. Calculation of absolute photosystem I absorption cross-sections from P700 photo-oxidation kinetics. *Photosynth Res* **29**, 23-35, doi:10.1007/BF00035203 (1991).
33 Ryan-Keogh, T. J., Macey, A. I., Cockshutt, A. M., Moore, C. M. & Bibby, T. S. The cyanobacterial chlorophyll-binding-protein Isia acts to increase the *in vivo* effective absorption cross-section of PSI under iron limitation(1). *J Phycol* **48**, 145-154, doi:10.1111/j.1529-8817.2011.01092.x (2012).
34 Odom, W. R., Hodges, R., Chitnis, P. R. & Guikema, J. A. Characterization of Synechocystis sp. PCC 6803 in iron-supplied and iron-deficient media. *Plant Mol Biol* **23**, 1255-1264, doi:10.1007/bf00042358 (1993).
35 Yadav, K. N. *et al.* Supercomplexes of plant photosystem I with cytochrome b6f, light-harvesting complex II and NDH. *Biochim Biophys Acta Bioenerg* **1858**, 12-20, doi:10.1016/j.bbabio.2016.10.006 (2017).
36 Steinbeck, J. *et al.* Structure of a PSI-LHCI-cyt b6f supercomplex in Chlamydomonas reinhardtii promoting cyclic electron flow under anaerobic conditions. *Proc Natl Acad Sci U S A* **115**, 10517-10522, doi:10.1073/pnas.1809973115 (2018).
37 Rast, A. *et al.* Biogenic regions of cyanobacterial thylakoids form contact sites with the plasma membrane. *Nat Plants* **5**, 436-446, doi:10.1038/s41477-019-0399-7 (2019).
38 Hellmich, J. *et al.* Native-like photosystem II superstructure at 2.44 A resolution through detergent extraction from the protein crystal. *Structure* **22**, 1607-1615, doi:10.1016/j.str.2014.09.007 (2014).
39 Umena, Y., Kawakami, K., Shen, J. R. & Kamiya, N. Crystal structure of oxygen-evolving photosystem II at a resolution of 1.9 A. *Nature* **473**, 55-60, doi:10.1038/nature09913 (2011).
40 Chang, L. *et al.* Structural organization of an intact phycobilisome and its association with photosystem II. *Cell Res* **25**, 726-737, doi:10.1038/cr.2015.59 (2015).
41 Zlenko, D. V., Galochkina, T. V., Krasilnikov, P. M. & Stadnichuk, I. N. Coupled rows of PBS cores and PSII dimers in cyanobacteria: symmetry and structure. *Photosynth Res* **133**, 245-260, doi:10.1007/s11120-017-0362-2 (2017).
42 McConnell, M. D., Koop, R., Vasil'ev, S. & Bruce, D. Regulation of the distribution of chlorophyll and phycobilin-absorbed excitation energy in cyanobacteria. A structure-based model for the light state transition. *Plant Physiol* **130**, 1201-1212, doi:10.1104/pp.009845 (2002).
43 Seelert, H., Dencher, N. A. & Müller, D. J. Fourteen Protomers Compose the Oligomer III of the Proton-rotor in Spinach Chloroplast ATP Synthase. *Journal of Molecular Biology* **333**, 337-344, doi:10.1016/j.jmb.2003.08.046 (2003).
44 Hahn, A., Vonck, J., Mills, D. J., Meier, T. & Kuhlbrandt, W. Structure, mechanism, and regulation of the chloroplast ATP synthase. *Science* **360**, doi:10.1126/science.aat4318 (2018).
45 Pogoryelov, D. *et al.* The oligomeric state of c rings from cyanobacterial F-ATP synthases varies from 13 to 15. *J Bacteriol* **189**, 5895-5902, doi:10.1128/JB.00581-07 (2007).
46 Strauss, M., Hofhaus, G., Schroder, R. R. & Kuhlbrandt, W. Dimer ribbons of ATP synthase shape the inner mitochondrial membrane. *EMBO J* **27**, 1154-1160, doi:10.1038/emboj.2008.35 (2008).
47 Daum, B., Nicastro, D., Il, J. A., McIntosh, J. R. & Kuhlbrandt, W. Arrangement of Photosystem II and ATP Synthase in Chloroplast Membranes of Spinach and Pea. *Plant Cell* **22**, 1299-1312, doi:10.1105/tpc.109.071431 (2010).
48 Schuller, J. M. *et al.* Structural adaptations of photosynthetic complex I enable ferredoxin-dependent electron transfer. *Science* **363**, 257-+, doi:10.1126/science.aau3613 (2019).
49 Laughlin, T. G., Bayne, A. N., Trempe, J. F., Savage, D. F. & Davies, K. M. Structure of the complex I-like molecule NDH of oxygenic photosynthesis. *Nature* **566**, 411-414, doi:10.1038/s41586-019-0921-0 (2019).
50 Arteni, A. A. *et al.* Structural characterization of NDH-1 complexes of Thermosynechococcus elongatus by single particle electron microscopy. *Biochim Biophys Acta* **1757**, 1469-1475, doi:10.1016/j.bbabio.2006.05.042 (2006).
51 Folea, I. M. *et al.* Single particle analysis of thylakoid proteins from Thermosynechococcus elongatus and Synechocystis 6803: localization of the CupA subunit of NDH-1. *FEBS Lett* **582**, 249-254, doi:10.1016/j.febslet.2007.12.012 (2008).
52 Birungi, M. *et al.* Possibilities of subunit localization with fluorescent protein tags and electron microscopy examplified by a cyanobacterial NDH-1 study. *Biochim Biophys Acta* **1797**, 1681-1686, doi:10.1016/j.bbabio.2010.06.004 (2010).

53 Peltier, G., Aro, E. M. & Shikanai, T. NDH-1 and NDH-2 Plastoquinone Reductases in Oxygenic Photosynthesis. *Annu Rev Plant Biol* **67**, 55-80, doi:10.1146/annurev-arplant-043014-114752 (2016).
54 Schuller, J. M. *et al.* Redox-coupled proton pumping drives carbon concentration in the photosynthetic complex I. *Nature Communications* **11**, 494, doi:10.1038/s41467-020-14347-4 (2020).
55 Kouril, R. *et al.* Structural characterization of a plant photosystem I and NAD(P)H dehydrogenase supercomplex. *Plant J* **77**, 568-576, doi:10.1111/tpj.12402 (2014).
56 Peng, L., Fukao, Y., Fujiwara, M., Takami, T. & Shikanai, T. Efficient operation of NAD(P)H dehydrogenase requires supercomplex formation with photosystem I via minor LHCI in Arabidopsis. *Plant Cell* **21**, 3623-3640, doi:10.1105/tpc.109.068791 (2009).
57 Gao, F. *et al.* The NDH-1L-PSI Supercomplex Is Important for Efficient Cyclic Electron Transport in Cyanobacteria. *Plant Physiol* **172**, 1451-1464, doi:10.1104/pp.16.00585 (2016).
58 Singh, A. K. & Sherman, L. A. Iron-independent dynamics of IsiA production during the transition to stationary phase in the cyanobacterium Synechocystis sp. PCC 6803. *FEMS Microbiol Lett* **256**, 159-164, doi:10.1111/j.1574-6968.2006.00114.x (2006).
59 Bibby, T. S., Nield, J. & Barber, J. Three-dimensional model and characterization of the iron stress-induced CP43'-photosystem I supercomplex isolated from the cyanobacterium Synechocystis PCC 6803. *J Biol Chem* **276**, 43246-43252, doi:10.1074/jbc.M106541200 (2001).
60 Kouril, R. *et al.* Photosystem I trimers from Synechocystis PCC 6803 lacking the PsaF and PsaJ subunits bind an IsiA ring of 17 units. *Biochim Biophys Acta* **1607**, 1-4, doi:10.1016/j.bbabio.2003.08.002 (2003).
61 Aspinwall, C. L., Duncan, J., Bibby, T., Mullineaux, C. W. & Barber, J. The trimeric organisation of photosystem I is not necessary for the iron-stress induced CP43' protein to functionally associate with this reaction centre. *FEBS Lett* **574**, 126-130, doi:10.1016/j.febslet.2004.08.016 (2004).
62 Kouril, R. *et al.* Supercomplexes of IsiA and photosystem I in a mutant lacking subunit PsaL. *Biochim Biophys Acta* **1706**, 262-266, doi:10.1016/j.bbabio.2004.11.008 (2005).
63 Sarcina, M. & Mullineaux, C. W. Mobility of the IsiA chlorophyll-binding protein in cyanobacterial thylakoid membranes. *J Biol Chem* **279**, 36514-36518, doi:10.1074/jbc.M405881200 (2004).
64 Riethman, H. C. & Sherman, L. A. Purification and characterization of an iron stress-induced chlorophyll-protein from the cyanobacterium Anacystis nidulans R2. *Biochim Biophys Acta* **935**, 141-151, doi:10.1016/0005-2728(88)90211-3 (1988).
65 Burnap, R. L., Troyan, T. & Sherman, L. A. The highly abundant chlorophyll-protein complex of iron-deficient Synechococcus sp. PCC7942 (CP43') is encoded by the isiA gene. *Plant Physiol* **103**, 893-902, doi:10.1104/pp.103.3.893 (1993).
66 Sandstrom, S., Park, Y. I., Oquist, G. & Gustafsson, P. CP43', the isiA gene product, functions as an excitation energy dissipator in the cyanobacterium Synechococcus sp. PCC 7942. *Photochem Photobiol* **74**, 431-437 (2001).
67 Zhang, J. *et al.* Structure of phycobilisome from the red alga Griffithsia pacifica. *Nature* **551**, 57-63, doi:10.1038/nature24278 (2017).
68 Liu, L. N., Chen, X. L., Zhang, Y. Z. & Zhou, B. C. Characterization, structure and function of linker polypeptides in phycobilisomes of cyanobacteria and red algae: An overview. *Biochimica et Biophysica Acta-Bioenergetics* **1708**, 133-142, doi:10.1016/j.bbabio.2005.04.001 (2005).
69 Arteni, A. A. *et al.* Structure and organization of phycobilisomes on membranes of the red alga *Porphyridium cruentum*. *Photosynth Res* **95**, 169-174, doi:10.1007/s11120-007-9264-z (2008).
70 Liu, L. N. *et al.* Light-induced energetic decoupling as a mechanism for phycobilisome-related energy dissipation in red algae: a single molecule study. *PLoS ONE* **3**, e3134 (2008).
71 Zhao, L. S. *et al.* Supramolecular architecture of photosynthetic membrane in red algae in response to nitrogen starvation. *Biochim Biophys Acta* **1857**, 1751-1758, doi:10.1016/j.bbabio.2016.08.005 (2016).
72 Green, B. R. What Happened to the Phycobilisome? *Biomolecules* **9**, doi:10.3390/biom9110748 (2019).
73 Straskova, A. *et al.* Pigment-protein complexes are organized into stable microdomains in cyanobacterial thylakoids. *Biochim Biophys Acta Bioenerg*, doi:10.1016/j.bbabio.2019.07.008 (2019).
74 Folea, I. M., Zhang, P., Aro, E. M. & Boekema, E. J. Domain organization of photosystem II in membranes of the cyanobacterium *Synechocystis* PCC6803 investigated by electron microscopy. *FEBS Lett* **582**, 1749-1754, doi:10.1016/j.febslet.2008.04.044 (2008).
75 Liu, L. N. *et al.* Watching the native supramolecular architecture of photosynthetic membrane in red algae: topography of phycobilisomes and their crowding, diverse distribution patterns. *J Biol Chem* **283**, 34946-34953, doi:10.1074/jbc.M805114200 (2008).

76 Lenn, T., Leake, M. C. & Mullineaux, C. W. Clustering and dynamics of cytochrome *bd*-I complexes in the *Escherichia coli* plasma membrane *in vivo*. *Mol Microbiol* **70**, 1397-1407, doi:10.1111/j.1365-2958.2008.06486.x (2008).
77 Llorente-Garcia, I. *et al.* Single-molecule *in vivo* imaging of bacterial respiratory complexes indicates delocalized oxidative phosphorylation. *Biochim Biophys Acta* **1837**, 811-824, doi:10.1016/j.bbabio.2014.01.020 (2014).
78 Johnson, A. S., van Horck, S. & Lewis, P. J. Dynamic localization of membrane proteins in *Bacillus subtilis*. *Microbiology* **150**, 2815-2824, doi:10.1099/mic.0.27223-0 (2004).
79 Cornejo, E., Abreu, N. & Komeili, A. Compartmentalization and organelle formation in bacteria. *Curr Opin Cell Biol* **26**, 132-138, doi:10.1016/j.ceb.2013.12.007 (2014).
80 Vogel, F., Bornhovd, C., Neupert, W. & Reichert, A. S. Dynamic subcompartmentalization of the mitochondrial inner membrane. *J Cell Biol* **175**, 237-247, doi:10.1083/jcb.200605138 (2006).
81 Watanabe, M. *et al.* Attachment of phycobilisomes in an antenna-photosystem I supercomplex of cyanobacteria. *Proc Natl Acad Sci U S A* **111**, 2512-2517, doi:10.1073/pnas.1320599111 (2014).
82 Iwai, M. *et al.* Isolation of the elusive supercomplex that drives cyclic electron flow in photosynthesis. *Nature* **464**, 1210-1213, doi:10.1038/nature08885 (2010).
83 Peng, L., Shimizu, H. & Shikanai, T. The chloroplast NAD(P)H dehydrogenase complex interacts with photosystem I in Arabidopsis. *J Biol Chem* **283**, 34873-34879, doi:10.1074/jbc.M803207200 (2008).
84 Lapuente-Brun, E. *et al.* Supercomplex assembly determines electron flux in the mitochondrial electron transport chain. *Science* **340**, 1567-1570, doi:10.1126/science.1230381 (2013).
85 Pan, X. *et al.* Structural basis for electron transport mechanism of complex I-like photosynthetic NAD(P)H dehydrogenase. *Nat Commun* **11**, 610, doi:10.1038/s41467-020-14456-0 (2020).
86 Zhang, C. *et al.* Structural insights into NDH-1 mediated cyclic electron transfer. *Nature communications* **11**, 888-888, doi:10.1038/s41467-020-14732-z (2020).
87 Katoh, H., Grossman, A. R., Hagino, N. & Ogawa, T. A gene of Synechocystis sp strain PCC 6803 encoding a novel iron transporter. *Journal of Bacteriology* **182**, 6523-6524, doi:Doi 10.1128/Jb.182.22.6523-6524.2000 (2000).
88 Wang, Q., Hall, C. L., Al-Adami, M. Z. & He, Q. IsiA is required for the formation of photosystem I supercomplexes and for efficient state transition in synechocystis PCC 6803. *PLoS One* **5**, e10432, doi:10.1371/journal.pone.0010432 (2010).
89 Gust, B., Kieser, T. & Chater, K. F. *REDIRECT Technology: PCR-targeting System in Streptomyces coelicolor*. (John Innes Centre, 2002).
90 Huang, F. *et al.* Roles of RbcX in carboxysome biosynthesis in the cyanobacterium *Synechococcus elongatus* PCC7942. *Plant Physiol* **179**, 184-194, doi:10.1104/pp.18.01217 (2019).
91 Li, M., Semchonok, D. A., Boekema, E. J. & Bruce, B. D. Characterization and Evolution of Tetrameric Photosystem I from the Thermophilic Cyanobacterium Chroococcidiopsis sp TS-821. *Plant Cell* **26**, 1230-1245, doi:10.1105/tpc.113.120782 (2014).
92 Zhang, P. P. *et al.* Expression and functional roles of the two distinct NDH-1 complexes and the carbon acquisition complex NdhD3/NdhF3/CupA/Sll1735 in Synechocystis sp PCC 6803. *Plant Cell* **16**, 3326-3340, doi:DOI 10.1105/tpc.104.026526 (2004).
93 Pettersen, E. F. *et al.* UCSF Chimera--a visualization system for exploratory research and analysis. *J Comput Chem* **25**, 1605-1612, doi:10.1002/jcc.20084 (2004).
94 Zhang, P. P. *et al.* Operon flv4-flv2 Provides Cyanobacterial Photosystem II with Flexibility of Electron Transfer. *Plant Cell* **24**, 1952-1971, doi:10.1105/tpc.111.094417 (2012).
95 Faulkner, M. *et al.* Direct characterization of the native structure and mechanics of cyanobacterial carboxysomes. *Nanoscale* **9**, 10662–10673, doi:10.1039/C7NR02524F (2017).